Available online at www.sciencedirect.com
SCIENCE DIRECT®
Icarus 172 (2004) 328–348
ICARUS
www.elsevier.com/locate/icarus

Gravitational accretion of particles in Saturn's rings

Raine Karjalainen *, Heikki Salo

Deptartment of Physical Sciences, Astronomy Division, PO BOX 3000, FI-90014, University of Oulu, Finland

Received 30 September 2003; revised 30 April 2004

Available online 3 August 2004

Abstract

Gravitational accretion in the rings of Saturn is studied with local N-body simulations, taking into account the dissipative impacts and gravitational forces between particles. Common estimates of accretion assume that gravitational sticking takes place beyond a certain distance (Roche distance) where the self-gravity between a pair of ring particles exceeds the disrupting tidal force of the central object, the exact value of this distance depending on the ring particles' internal density. However, the actual physical situation in the rings is more complicated, the growth and stability of the particle groups being affected also by the elasticity and friction in particle impacts, both directly via sticking probabilities and indirectly via velocity dispersion, as well as by the shape, rotational state and the internal packing density of the forming particle groups. These factors are most conveniently taken into account via N-body simulations. In our standard simulation case of identical 1 m particles with internal density of solid ice, $\rho = 900\ \mathrm{kg\,m^{-3}}$, following the Bridges et al., 1984 elasticity law, we find accretion beyond $a = 137{,}000$–$146{,}000$ km, the smaller value referring to a distance where transient aggregates are first obtained, and the larger value to the distance where stable aggregates eventually form in every experiment lasting 50 orbital periods. Practically the same result is obtained for a constant coefficient of restitution $\epsilon_n = 0.5$. In terms of r_p parameter, the sum of particle radii normalized by their mutual Hill radius, the above limit for perfect accretion corresponds to $r_p < 0.84$. Increased dissipation ($\epsilon_n = 0.1$), or inclusion of friction (tangential force 10% of normal force) shifts the accretion region inward by about 5000 km. Accretion is also more efficient in the case of size distribution: with a $q = 3$ power law extending over a mass range of 1000, accretion shifts inward by almost 10,000 km. The aggregates forming in simulations via gradual accumulation of particles are synchronously rotating.

Keywords: Planetary rings, Saturn; Accretion

1. Introduction

Although the main bulk of Saturn ring's mass is assumed to reside in particles in 1–5 m radius range, there are some indirect observational evidence of larger aggregates (Showalter and Nicholson, 1990; Showalter, 1998; French and Nicholson, 2000). F ring contains arcs (Nicholson et al., 1996; Charnoz et al., 2001) and bodies that are assumed to be clumps of smaller particles (Bosh and Rivkin, 1996; Roddier et al., 2000; McGhee et al., 2001). Showalter (1998) found from Voyager images that the longitudinal brightness showed short lived brightenings, which he interpreted to result from micro-meteoroid bombardment to moonlets that have dust on their surface. Later Poulet et al. (2000) and Barbara and Esposito (2002) explained these bursts as a result from collisions between the moonlets in the core of the F ring. So, there are plenty of reasons to believe that clumps or smaller moonlets exist in Saturn's rings even though none have yet been directly detected. Dynamical N-body models (Salo, 1992b, 1995) also indicate a gravitational growth of particle aggregates in the outer parts of the rings, provided that the internal density of particles is not much below that of solid ice. These results are also supported by 3-body orbital integrations (Ohtsuki, 1993; Morishima and Salo, 2004).

Historically, the boundary between ring and satellite region has been discussed in terms of Roche limit. The classical Roche limit refers to an idealized situation of a synchro-

* Corresponding author. Fax: +358-8-553-1934.
E-mail address: raine.karjalainen@oulu.fi (R. Karjalainen).

0019-1035/$ – see front matter
doi:10.1016/j.icarus.2004.05.022

nously rotating liquid satellite (i.e., a body without material strength), distorted by tidal and centrifugal forces. In 1847 Roche showed (see Chandrasekhar, 1969) that the critical minimum value for the orbital radii a inside which no closed equipotential surface can exist is

$$\frac{a}{R_\mathrm{p}} = 2.456\left(\frac{\rho_\mathrm{p}}{\rho}\right)^{1/3}, \tag{1}$$

where R_p and ρ_p are the mean radius and density of the planet, while ρ denotes the density of the satellite. However, if an actual satellite with a non-zero internal strength were brought toward the planet, it would survive tidal forces even at much closer distances (Aggarwal and Oberbeck, 1974).

Likewise, ring particles are located inside the classical Roche limit, but accretion can still take place, provided that the net attraction between a pair of particles in contact is toward each other. When two radially aligned solid spherical particles with the same internal density and equal size rotate synchronously, the net attraction is zero at

$$\frac{a}{R_\mathrm{p}} = 2.29\left(\frac{\rho_\mathrm{p}}{\rho}\right)^{1/3}. \tag{2}$$

When we have a small particle on the surface of a much larger synchronously rotating particle, there is no net attraction at

$$\frac{a}{R_\mathrm{p}} = 1.44\left(\frac{\rho_\mathrm{p}}{\rho}\right)^{1/3} \tag{3}$$

(Weidenschilling et al., 1984; Davis et al., 1984). For ice, with internal density $\rho = 900\ \mathrm{kg\,m^{-3}}$, the estimates (2) and (3) correspond to 122,000 and 77,000 km for Saturn's rings. These can be compared to semianalytical criteria derived by Ohtsuki (1993) and expressed in terms of r_p. These limiting distances are identical to those for attaining $r_\mathrm{p} = 1$, where r_p is the sum of the particle radii scaled by their mutual Hill-radius (the semilength of the Hill-surface in the radial direction)

$$r_\mathrm{p} = (r_1 + r_2)/R_\mathrm{Hill}, \tag{4}$$

where

$$R_\mathrm{Hill} = a\left(\frac{m_1 + m_2}{3M}\right)^{1/3}, \tag{5}$$

r_1, r_2, m_1, and m_2 denoting the radii and masses of the small particles rotating about the central object with a mass M. For Saturn's rings we can write (Salo, 1995)

$$r_\mathrm{p} = 0.77\left(\frac{\rho}{900\ \mathrm{kg\,m^{-3}}}\right)^{-1/3}\left(\frac{a}{10^8\ \mathrm{m}}\right)^{-1}\frac{1+\mu^{1/3}}{(1+\mu)^{1/3}}, \tag{6}$$

where $\mu = m_1/m_2$ is the mass ratio of the particles.

However, the condition $r_\mathrm{p} = 1$ has only limited relevance for the actual sticking of particles, or to the stability of the formed aggregates, as it refers to a particle pair with a specific mutual orientation, and with zero relative velocity. A more realistic estimate for sticking, taking into account the mutual velocities and different impact directions of the colliding particles, was obtained by Ohtsuki (1993). He used the condition that the Hill-energy of the pair after an impact (or a sequence of impacts) needs to be negative for the pair to become bound. He showed, in terms of 3-body integrations, that the sticking probability depends significantly on the velocity dispersion, and on the elasticity of impacts. Especially, the probability drops rapidly toward zero for $r_\mathrm{p} > 2/3$, in which case the pair extends partially outside its Hill-surface. In the realistic case of particle ensembles the situation is further complicated by the fact that the velocity dispersion itself is determined by the impacts and gravitational encounters between particles. Collective gravitational effects may also be important for accretion (Salo, 1992b). Moreover, the accretional evolution and the evolution of velocity dispersion are coupled, as any forming aggregates will heat the system via gravitational scattering. The interaction between the aggregates themselves may also affect their growth.

In this study we address the onset of gravitational accretion in the outer parts of Saturn's rings via numerical N-body simulations, which at least to some degree allow for all the above mentioned complications. Our goal is to look how different factors affect the distance beyond which accretion becomes possible. Section 2 describes briefly the main ingredients of the computational method. In Section 3 we discuss the detection of aggregates in simulations, and in Section 4 results from an extensive series of N-body experiments are reported. Finally, Section 5 summarizes our results.

2. N-body simulation method

We use the local simulation method (Wisdom and Tremaine, 1988; Salo, 1991, 1992a, 1992b, 1995), to study the conditions for the onset of accretion. Collisions and gravitational interactions between the ring particles are both taken into account. All calculations are restricted to a small comoving region inside the ring, orbiting with the circular angular velocity Ω at the distance a (see Fig. 1). The particles leaving the calculation region are treated in terms of periodic boundary conditions which take into account the systematic shear in the radial direction. Thus each time a particle leaves the calculation region, one of its image particles enters it, with appropriately modified tangential velocity. Linearized equations of motion are employed, for the $i = 1, \ldots, N$ particles with position vectors $\bar{R}_i \equiv (x_i, y_i, z_i)$ and masses m_i,

$$m_i\left(\ddot{x}_i - 2\Omega\dot{y}_i - 3\Omega^2 x_i\right) = F_x^g + F_x^\mathrm{imp}, \tag{7}$$

$$m_i\left(\ddot{y}_i + 2\Omega\dot{x}_i\right) = F_y^g + F_y^\mathrm{imp}, \tag{8}$$

$$m_i\left(\ddot{z}_i + \Omega^2 z_i\right) = F_z^g + F_z^\mathrm{imp}, \tag{9}$$

where the x-axis points to the radial direction, the y-axis in the direction of mean orbital motion and z-axis completes a right-handed coordinate system. Equations (7)–(9) are valid when $x/a \ll 1, y/a \ll 1, z/a \ll 1$, which conditions are

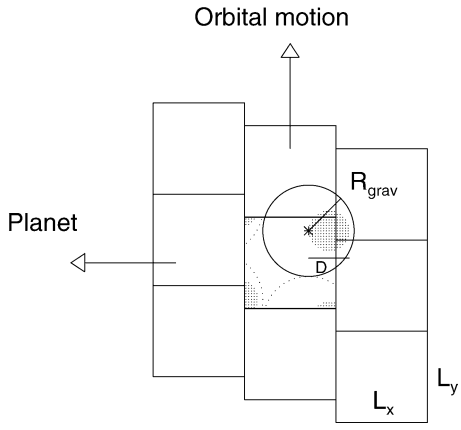

Fig. 1. *Schematic representation of the accretion simulation*. The local calculation cell (thick lines) and its surrounding eight nearest replicas are shown, L denoting the width of the square-shaped calculation region. The dashed region represents a particle clump with a longest diameter D, extending partially over the periodic borders of the calculation region. The solid circle gives an example of the gravity calculation region with radius $R_{\rm grav}$, around one of the particles in the clump (marked by the asterisk). Dashed lines indicate how the gravity calculation region is copied to the original calculation cell. $R_{\rm grav}$ has two restrictions: (1) $R_{\rm grav} > D$, to assure that each particle of the aggregate feels the gravity from all its other particles, and (2) $R_{\rm grav} < L - D$, in order to prevent the clump from feeling the gravity from its own image, over the periodic borders. Depending on the number of simulation particles N, the used $R_{\rm grav}$ range between 30–70 particle radii (for $N = 500$–5000, respectively).

safely fulfilled in rings. The force in the right-hand side includes the forces affecting the particles during the impacts, $\vec{F}^{\rm imp}$, as well as the mutual gravitational forces

$$\vec{F}_i^g = \sum_{\substack{j=1 \\ j\neq i}}^{N} -Gm_i m_j \frac{R_{ij}}{r_{ij}^3}, \tag{10}$$

where $\vec{R}_{ij} \equiv \vec{R}_i - \vec{R}_j$ and $r_{ij} \equiv |\vec{R}_{ij}|$.

In our recent simulations of dense planetary rings (Salo et al., 2001; Schmidt et al., 2001) we have calculated the ring self-gravity by using a particle–particle method for nearby gravity, combined with a particle–mesh calculation of the influence of more distant particles. Since the latter contribution can be evaluated with the help of FFT, this made it feasible to achieve a large number of particles, $N \sim 10^4$–10^5, required for a realistic study of overstability in self-gravitating dense rings. In the present study, involving an extended survey of parameter space, we limit to a fairly small number of particles, $N \leqslant 5000$, and to avoid any possible inaccuracy related to the grid-based force evaluation, calculate the self-gravity by direct summation, over all particle pairs within a given limiting distance $R_{\rm grav}$. As explained in Salo (1995), the nearest images are considered in calculations for each particle pair. The radius of the gravity calculation region, $R_{\rm grav}$, has two restrictions,

$$D_{\rm clump} < R_{\rm grav} < \min\left[\frac{L}{2}, L - D_{\rm clump}\right], \tag{11}$$

where L is the total width of the square-shaped simulation region and $D_{\rm clump}$ is the maximum diameter of the aggregate which can form with N particles. The lower limit is included to make sure that each particle in the aggregate feels the gravity of the every other particle in the same aggregate, whereas the upper limit prevents the image clumps (i.e., the copies of the same aggregate in the adjacent image regions) from disturbing the aggregate we are studying. In practice, the value of $D_{\rm clump}$ depends, besides N, on the shape and porosity of the forming aggregate; suitable values for $R_{\rm grav}$ fulfilling the condition (11) were determined via preliminary simulations. Note, however, that due to limited $R_{\rm grav}$ the present experiments underestimate the long-range gravitational effects, like the formation of gravitational wake structures (see Section 4.2.3) or the tidal interaction between distinct clumps, if several large clumps form in the calculation region.

The collisions between particles are modeled with the force method (Salo, 1995), mimicking the actual viscoelastic and frictional forces between impacting particles. In the case of self-gravitating particles this method is clearly superior over the often used method of treating impacts as instantaneous velocity changes (see, e.g., Wisdom and Tremaine, 1988; Salo, 1987, 1991, 1992a, 1992b; Richardson, 1994), as no extra treatment is needed for preventing artificial particle overlaps. Also, the mere concept of individual impacts has no meaning if the gravity is strong enough to lead to particle sticking. Denoting by $\vec{R}$ and $\vec{R}'$ the radius vectors of the two colliding particles, the mutual impact force is divided into normal and tangential components

$$\vec{F}^{\rm imp} = F_{\rm n}\vec{c} + F_{\rm t}\vec{c}_{\rm t}, \tag{12}$$

where $\vec{c} = (\vec{R} - \vec{R}')/|\vec{R} - \vec{R}'|$, is the unit vector in the direction joining the particle centers, and $\vec{c}_{\rm t}$ the unit vector in the direction of the component of the instantaneous velocity difference along the tangent plane of impact. The relative acceleration of particles is determined by

$$\bar{M}\left(\ddot{\vec{R}} - \ddot{\vec{R}}'\right) = \vec{F}^{\rm imp}, \tag{13}$$

where $\bar{M} = mm'/(m + m')$ is the effective mass of the pair: the accelerations of individual particles follow from the conservation of linear momentum. The normal force component is composed of a restoring harmonic force and a viscous damping force (Dilley, 1993),

$$F_{\rm n}(\xi) = \begin{cases} k\xi + \beta\dot{\xi}, & \xi > 0, \\ 0, & \xi \leqslant 0, \end{cases} \tag{14}$$

where $\xi = (r + r') - |\vec{R} - \vec{R}'|$ is the penetration depth ($\xi \ll r + r'$) during impact, r and r' denoting the radii of the impacting particles. The spring constant of the harmonic force, $k/\bar{M}$, and the dissipation parameter, $\beta/\bar{M}$, are tied to simple physical parameters defining the outcome of the impact: they are chosen in a manner that yields a desired duration of the impact, $T_{\rm dur}$, and a pre-determined value for the normal coefficient of restitution, $\epsilon_{\rm n}$, defined as the ratio

of post and pre-collisional perpendicular velocity difference. Especially,

$$T_{\rm dur} \approx \pi/\omega_0, \tag{15}$$

where $\omega_0 = \sqrt{k/\bar{M}}$ is the undamped frequency of the harmonic impact force (see Salo, 1995, for details).[1] Later in this section we discuss how to choose $T_{\rm dur}$ in a manner that assures that the results are independent of this simulation parameter, while still keeping the total computing time manageable.

In the case surface friction is included, the particle spins need also to be taken into account, since due to the torque affecting at the impact point there is a transfer of energy between translational and rotational degrees of freedom (see, e.g., Salo, 1987). The most often used method to describe friction (e.g., Salo, 1987; Longaretti, 1989; Hämeen-Anttila and Salo, 1993) is in terms of tangential coefficient of restitution $\epsilon_{\rm t}$, defined in terms of the change in the tangential velocity difference, in an analogous manner as $\epsilon_{\rm n}$. However, here we model friction by assuming that the tangential component of force between the colliding particles is proportional to the normal force,

$$F_{\rm t} = -k_{\rm f} F_{\rm n}, \tag{16}$$

where $k_{\rm f} \geqslant 0$ is the coefficient of friction. This treatment again has the advantage that it can also be applied in the case of gravitational sticking of particles, where the definition of instantaneous velocity change becomes ambiguous. The frictional force acts in the direction opposite to the instantaneous velocity difference along the impact plane, $c_{\rm t} = (\vec{v}_{\rm coll} - \vec{v}_{\rm coll}\cdot\vec{c})/|\vec{v}_{\rm coll} - \vec{v}_{\rm coll}\cdot\vec{c}|$, with

$$\vec{v}_{\rm coll} = \vec{v} - \left(r(\vec{\omega} - \vec{\Omega}) + r'(\vec{\omega}' - \vec{\Omega})\right) \times \vec{c}, \tag{17}$$

where $\vec{v} = \dot{\vec{R}} - \dot{\vec{R}}'$ is the velocity difference between the particle centers and $\vec{\omega}$ and $\vec{\omega}'$ denote the spin vectors of the particles, measured in the inertial frame, and $\vec{\Omega}$ is the angular velocity vector of the rotating coordinate system: $\vec{\omega} - \vec{\Omega}$ and $\vec{\omega}' - \vec{\Omega}$ thus represent the spin vectors in the rotating frame. The accelerations of the spin vectors due to impact torque depend on the internal mass distribution of particles: we treat the particles as homogeneous spheres, with a moment of inertia $2/5 m_i r_i^2$, in which case

$$mr\dot{\vec{\omega}} = m'r'\dot{\vec{\omega}}' = -\frac{5}{2} k_{\rm f} F_{\rm n} \vec{c} \times \vec{c}_{\rm t}. \tag{18}$$

Similar model for friction was recently utilized in Morishima and Salo (2004): note, however that their friction parameter $l_{\rm f}$ corresponds to $\frac{7}{2}k_{\rm f}$.

[1] Strictly speaking, $T_{\rm dur}$ and $\epsilon_{\rm n}$ refer to an impact between two particles in a free space without any additional forces. However, these quantities can be utilized to determine the values of the parameters in Eq. (14), applicable also in the case of gravitational sticking of particles.

Most of our simulations employ a velocity-dependent normal coefficient of restitution,

$$\epsilon_{\rm n}(v_{\rm n}) = \max\left[\left(\frac{v_{\rm n}}{v_c}\right)^{-0.234}, 0.25\right], \tag{19}$$

when $v_{\rm n} > v_c$, otherwise $\epsilon_{\rm n}(v_{\rm n})$ is set to unity. According to Bridges et al. (1984) laboratory measurements this type of relation with $v_c \approx 0.0077$ cm s^{-1} represents well the behavior of frost covered ice at low temperatures. Also simulations with constant $\epsilon_{\rm n} = 0.1$ and 0.5 were performed. The choice of the friction coefficient is more problematic, since relevant laboratory measurements exist only for the tangential coefficient of restitution $\epsilon_{\rm t}$. Considering the change of tangential and normal velocity components in impacts, $v_{\rm t} = |\vec{v}_{\rm coll} - v_{\rm n}\vec{c}|$ and $v_{\rm n} = \vec{v}\cdot\vec{c}$, one obtains

$$k_{\rm f} = \frac{2}{7}\frac{(1-\epsilon_{\rm t})v_{\rm t}}{(1+\epsilon_{\rm n})v_{\rm n}}. \tag{20}$$

Thus, there is no one-to-one correspondence between $k_{\rm f}$ and $\epsilon_{\rm t}$, their relation depending on the direction of the impact. According to Supulver et al. (1995), $\epsilon_{\rm t} \approx 0.9$ for glancing 1 cm/sec impacts of ice particles, which indicates a rather small $k_{\rm f}$, perhaps of the order of 0.01–0.1.

In the force method the particle orbits through each impact are numerically integrated, and a certain minimum number of steps per impact duration is needed for a sufficient accuracy. At the same time, the total number of simulation steps is determined by orbital timescales. Therefore, using a very small impact duration would imply excessive CPU time-consumption. The main advantage of the chosen linear force model, in comparison to more realistic, physically motivated models (see, e.g., the Hertzian impact model discussed in Spahn et al., 1995), is that in the linear model the duration of the impact is independent of impact velocity, and can be easily scaled to any desired value, by modifying ω_0. Thus instead of using actual impact durations of $\lesssim 1$ sec (Bridges et al., 2001), we typically employ impact durations which are about a factor of 50 larger. This allows a significant reduction in the required total number of simulation steps, while the impact duration is still short enough to prevent the orbital motion or self-gravity during the impact from causing $\epsilon_{\rm n}$ to deviate significantly from that in the case of more realistic short impact duration.

The orbital integrations are carried out with RK4 (fourth-order Runge–Kutta integrator), employing time steps of the order of 10^{-5} orbital periods (to ensure about 50 steps/impact duration). However, to speed up the calculations, self gravitational forces are updated less frequently, typically every $\Delta T \sim 10^{-3}$ orbital periods. Since the typical relative movements between particles during ΔT are only a few percent of particle radii, our original calculations treated self-gravitational forces fixed during ΔT. Here we followed the earlier simulations in Salo (1995), which showed that this approximation works well even in the case of moderately strong self-gravity, regarding the details of wake structure or the initial formation of particle aggregates. However, during

the course of the present study we noted that this approximation is unsuitable for following the long-term evolution of aggregates, since in the case of aggregates it introduces a secular energy input proportional to ΔT (see Appendix A), which eventually leads to an artificial rotational instability of the formed aggregates. A simple remedy is to replace the constant gravity during ΔT with a linear approximation,

$$\vec{F}_g = \vec{F}_g(t_0) + \dot{\vec{F}}_g(t - t_0), \quad (t - t_0) < \Delta T, \tag{21}$$

where $\dot{\vec{F}}_g$ is calculated by taking into account the particle positions and velocities at the time t_0. Since $\dot{\vec{F}}_g$ can be constructed at the same time as $\vec{F}_g$ itself is calculated, this means a very small extra CPU time consumption. In the case of an aggregate, the remaining secular energy error is proportional to ΔT^3, having no practical significance in comparison to other inaccuracies in simulations.

We also study how the inclusion of particle size distribution affects the onset of gravitational accretion. In these experiments a power-law size distribution is used,

$$dN/dr \propto r^{-q}, \tag{22}$$

where $q = 3$ and $0.5\ \text{m} < r < 5.0\ \text{m}$. In principle, the gravitational sticking of unequal sized particles is easier than that of equal-size particles (see Eqs. (2)–(4)), although this tendency is to some degree opposed by the larger velocity dispersion achieved by the small particles in a system with a mixture of sizes. For the maximal mass ratio of simulation particles, $\mu = 1000$, the r_p parameter is about 0.69 times that for an identical particle pair with $\mu = 1$, for a fixed distance and internal density. According to Voyager I radio occultation measurements (Marouf et al., 1983) the size distribution in Saturn's rings can be approximated by this type of power-law, though with a considerably smaller lower cut-off size ~ 1 cm. In this case, the maximal reduction of r_p parameter is slightly larger, being practically identical to that for $\mu \to \infty$, or about 0.63. Thus, although our size range is heavily truncated, it should still mimic fairly well the effects of a realistic, more extended size range. Likewise, the mass range of 1000 should already be wide enough to yield an almost asymptotic value for the ratio of velocity dispersions between the smallest and largest particles of the size distribution (see Salo, 1992a).

In our standard simulation model $N = 500$ identical particles with 1-m radius are simulated, using the Bridges et al. velocity-dependent elasticity model, with no friction, $k_\text{f} = 0$. The optical depth $\tau = 0.25$ and the internal density of particles is $900\ \text{kg m}^{-3}$, yielding a surface density of $300\ \text{kg m}^{-2}$. The time step ΔT for gravitational calculation is 0.001 orbital periods, and the spring constant in impact calculations corresponds to $\omega_0/\Omega = 400$ (impact duration $T_\text{dur} = 1/800$ orbital periods). In what follows, we vary in turn each of the parameters of this standard model, and observe how the accretion tendency is modified: both the parameters related to the simulation method ($\Delta T, \omega_0, N$), and the physical parameters ($\epsilon_\text{n}, k_\text{f}, dN/dr, \tau$) are studied. Since the accretion is statistical in nature, a series of 20 simulations is performed for each set of parameters, varying the seed of the random number generator in the creation of the initial particle positions and velocities. The simulations are performed for saturnocentric distances between 120,000–150,000 km (r_p between 1.0–0.8, respectively), the exact range depending on the parameter values, chosen to cover the distances from regions where no accretion is observed to distances where accretion occurs in every simulation.

3. Detecting accretion in simulations

In the case of flattened planetary rings the self-gravity between particles promotes the grouping of particles. This gravitational instability is opposed by the particles' random velocity dispersion and by the differential rotation, tending to dissolve any forming condensations. As long as the Toomre parameter (Toomre, 1964),

$$Q = \frac{c_r \Omega}{3.36 G \Sigma}, \tag{23}$$

where c_r is the radial velocity dispersion and G is the gravitational constant, exceeds at least a few times unity, the collective gravitational instability is completely avoided, and the system remains practically uniform: the effect of gravity is seen mainly in the enhanced impact frequency, and in the increased velocity dispersion induced by individual binary encounters. This is the case for low optical depth rings (Σ is small), or for rings located near the planet (Ω is large). However, if the optical depth and thus Σ increases, or if a ring location further away from the planet is inspected, so that Q falls below about 2, the collective gravity together with differential rotation leads to the formation of shearing tilted wake structures, individual wakes forming and dissolving in a time scale $\sim$ orbital period. These wakes are analogous to the transient wakes produced by orbiting mass enhancements in a stellar disk (Julian and Toomre, 1966; Toomre and Kalnajs, 1991), except that due to dissipative impacts between particles, the system is able to oppose the gravitational heating induced by the wakes themselves, leading to a statistical steady-state with a continuous regeneration of new wakes. The average tilt angle of wakes with respect to tangential direction is determined by the gradient of the systematic velocity field, corresponding to about 20° for the Keplerian case; the typical radial spacing between wakes is close to Toomre's critical wavelength (Toomre, 1964)

$$\lambda_\text{cr} = 4\pi^2 G \Sigma/\kappa^2, \tag{24}$$

where the epicyclic frequency κ equals Ω for the Keplerian case. For Saturn's A ring the expected $\lambda_\text{cr} \sim 50$–$100$ m.

As the strength of gravity relative to the tidal force further increases with an increased planetocentric distance, the wakes, besides becoming gradually stronger, also start to show an increased tendency for degrading into local clumps.

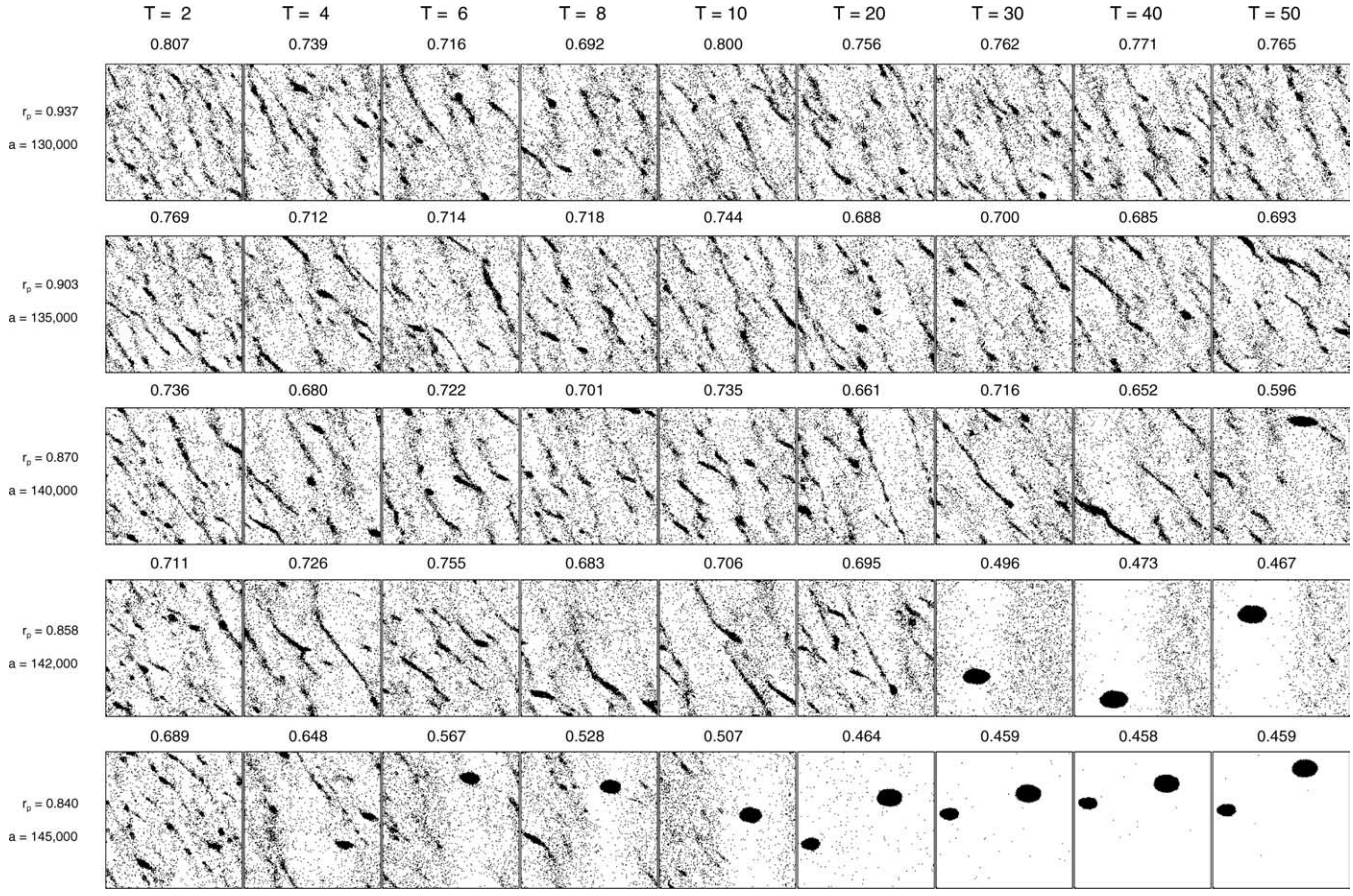

Fig. 2. Examples of simulations performed for different saturnocentric distances. Standard simulation values, i.e., identical particles, velocity-dependent coefficient of restitution, $\tau = 0.25$, and $k_f = 0$ are used, except that $N = 5000$. The size $L = 250$ m. For comparison, $L/\lambda_{cr} = 5.48$ and 3.95 for $a = 130{,}000$ and 145,000 km, respectively. The numbers on top of each frame indicate the value of H_q, calculated with $q_H = 5$, $m_x = m_y = 32$.

This tendency follows from the gravitational sticking of individual particles, as the r_p parameter for the particle pair (or a particle and a wake) falls below unity. Similar pairwise sticking of particles, leading to a formation of particle clumps, takes place also in low optical depths, without a formation of collective wake structures. Typical examples of both wakes and particle accretion are displayed in Fig. 2, see also Salo (1995), Daisaka and Ida (1999), Daisaka et al. (2001), and Ohtsuki and Emori (2000) for more examples of the wake structure.

Defining accretion with visual detection from simulation snapshots is somewhat subjective. Beyond a certain distance, the clumps eventually merge into a one or few aggregates, containing practically all simulation particles: in this case the detection of accretion is unambiguous. However, slightly inside this distance there is a transition zone, where it is hard to distinguish between a temporary, radially elongated aggregate and a wake, especially if the latter happens to have an almost radial temporary orientation. Also, the time scale for the formation of aggregates can become very long, exceeding the reasonable length of simulations.

Altogether, we have been experimenting with three different methods for defining accretion in simulations, with the first two related to a subjective detection of particle clumps:

(1) The first method is based on the criteria that a distinct particle clump (containing at least tens of particles in contact) must survive for a certain minimum number of orbital periods. If this is the case, the simulation is counted among those producing at least temporary accretion. Performing several simulations with the same distance and parameter values, we can then define a probability of accretion corresponding to this distance, by dividing the number of simulations where aggregates are detected by the total number of simulations (typically 20).
(2) In the second, closely related method, the time interval in the simulation where an aggregate is present is recorded. The accretion probability is defined as the total occurrence time interval of aggregates, in 20 separate simulations, divided by the total duration of these simulations.

In both methods, the snapshots corresponding to the initial evolution are discarded, to avoid the sensitivity to exact starting conditions. In the standard case with $\tau = 0.25$, or with $\tau > 0.25$, we discard the first 10 orbital periods, after which time the system has already achieved a statistical steady-state independent of initial values; for $\tau = 0.1$

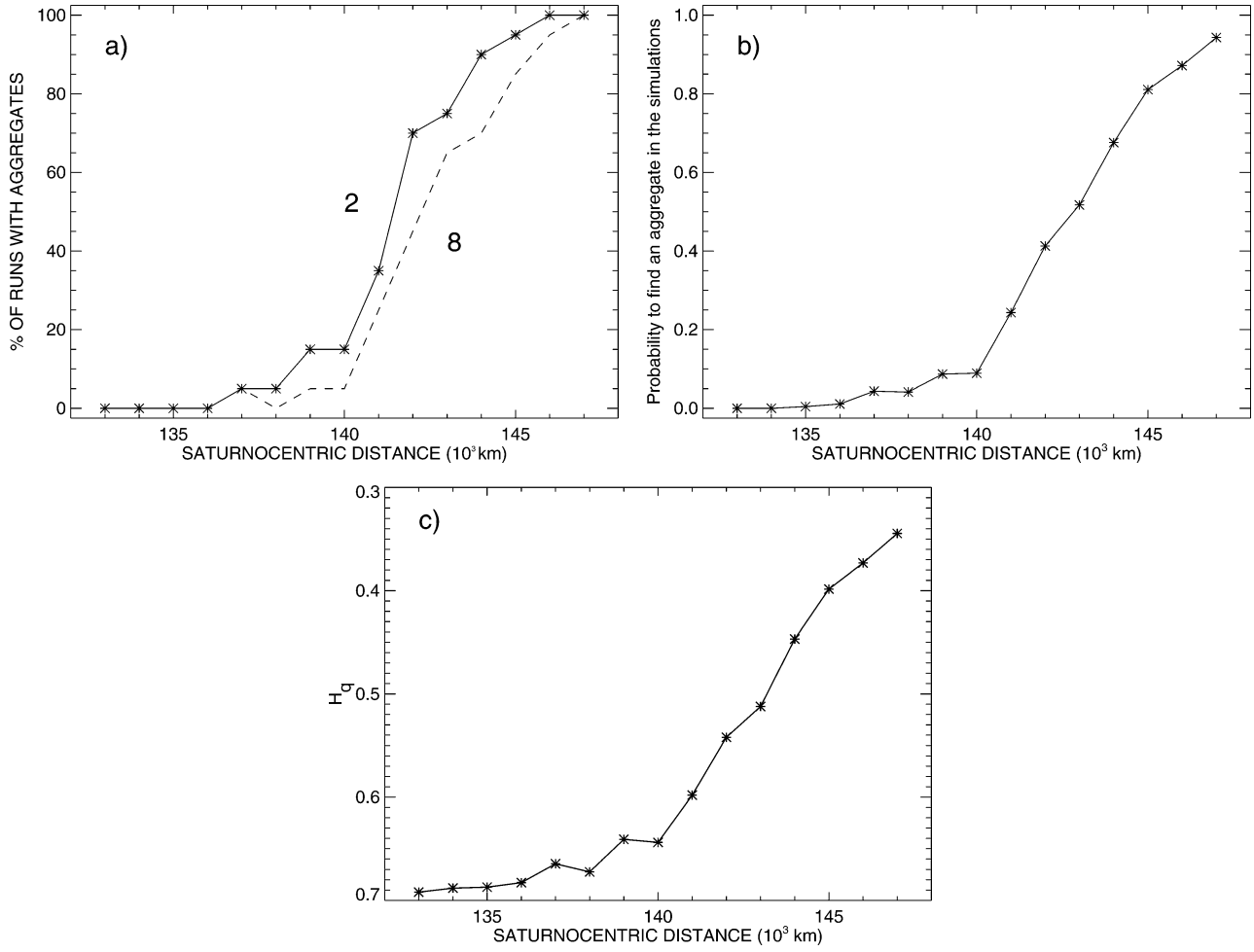

Fig. 3. Comparison of different methods for measuring accretion in simulations. The standard parameter values are used (the same as in Fig. 2, except with $N = 500$). For each distance 20 simulations with different seed were performed, each lasting 50 orbital periods. In each case, the 10 initial orbital periods are discarded from the analysis. (a) The fractional number of simulations leading to accretion. A simulation run was counted among those leading to accretion if at least one distinct particle clump was detected in visual inspection of simulation snapshots, surviving at least two (solid line), or eight (dashed line) orbital periods. (b) The fractional time aggregates were present in simulations, based on the same visual inspection as used in frame (a). (c) The average value of Renyi entropy H_q (Eq. (25)), measuring the clumpiness of the particle distribution: smaller values of H_q indicate larger deviations from uniform distribution). The parameters $m_x = m_y = 10$ and $q_H = 5$ are adopted. Although H_q does not distinguish between a tilted wake, and a more or less spherical aggregate, the trend is similar to that in frames (a) and (b), showing that H_q provides an objective way for detecting aggregate formation.

and 0.05, we discard 16 orbital periods. The detection of clumps is based mainly on snapshots of particle positions stored every two orbital periods, but to assure the identity of the clump, also other indicators like the impact frequency and velocity dispersion (stored about 10 times/orbital period) are utilized. Since the typical time scale of individual strong wakes is only of the order of one orbital period, a clump seen in two consecutive snapshots is almost always a genuine temporary aggregate, and not a misidentified wake. Also, requiring the clump to survive, say 8 orbital periods instead of 2, leads to essentially similar result. The first two frames in Fig. 3 show the results of these two methods, for our standard simulation case.

(3) The third, more objective way to study accretion is to use Renyi entropy (see, e.g., Spahn et al., 1997, who used it in their study of clustering of granular assemblies). For the calculation of Renyi entropy each simulation snapshot is divided into $m = m_x \times m_y$ rectangular subregions, and the number of particles in each subregion is registered. The normalized Renyi entropy is then defined as

$$H_q = \frac{1}{1 - q_H} \frac{\log \sum_{l=1}^{m} p_l^{q_H}}{\log m}, \tag{25}$$

where p is the probability of finding an particle in the in lth sub-box, and the exponent $q_H > 1$. Thus, if the particles are uniformly distributed, $p \approx 1/m$, implying $H_q \approx 1$, whereas if the particles are non-uniformly distributed, H_q is reduced, H_q reaching zero if all particles become concentrated in just one subregion. Although H_q in itself does not directly distinguish between a wake and a particle group, it proves out to be a valuable objective method for detecting the increased clumpiness associated with the degradation of wakes into aggregates: from Fig. 3 (the frame in the right) we can see

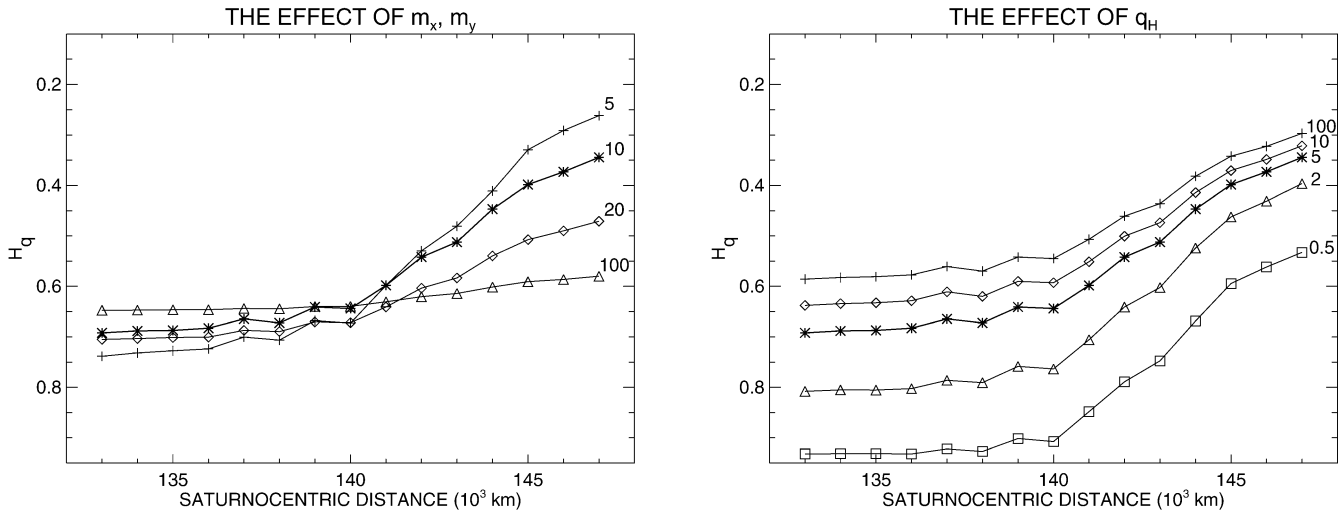

Fig. 4. (Left) The standard simulation series of Fig. 3 is used for checking how the number of subdivisions $m = m_x \times m_y$ affects the obtained H_q values. Labels indicate the value of $m_x = m_y$. The thick line with asterisks indicates the chosen standard values, used in all subsequent plots. (Right) The dependence of H_q on q_H, for $m_x = m_y = 10$. Thick line again shows the adopted value $q_H = 5$.

that Renyi entropy gives very similar results compared to methods based on visual detection of the aggregates. Like in the two other frames, the first 10 orbital periods of the initial evolution are discarded, the shown values corresponding to $\langle H_q \rangle$ during the rest of the run.

For a given particle distribution the numerical value of H_q depends on the number of sub-regions m and the exponent q_H. For example, this concerns the background level for small a, corresponding to the statistical graininess of the system in the presences of wakes, and the magnitude of the change in H_q which takes place when wakes transform to clumps with increasing distance. However, the qualitative trend of H_q with distance, in runs performed with a fixed number of particles, is not sensitive to the exact choice of these parameters (see Fig. 4). For our standard $N = 500$ particle case we choose $q_H = 5$, and $m = 100$, corresponding to the average number of 5 particles/subregion. In general, runs with different elastic properties (using the same N) can be directly compared with the same m and q_H. The situation is more complicated when systems with different number of particles are compared. In this case m is again chosen to yield the same average number of 5 particles/subregion. The value for the exponent q_H, however, is adjusted separately for each case, in a manner that yields the same H_q in a corresponding *non-self-gravitating* run. This makes the levels of H_q between different N's comparable in the region of small a (except for the differences due to different strengths of wakes), and the distances where H_q's start to change abruptly due to formation of clumps are easily detected (note that we do not care about the amplitude of the change in H_q in the accretion region as this depends on q_H).

Finally, it must be noted that the Renyi entropy does not have any special physical significance. For example, the particle auto-correlation function would certainly provide more accurate means for the detection and characterization of particle aggregates, being however much more time consuming to calculate. To give a visual impression of the meaning of H_q values, Fig. 5 compares the time-evolution of H_q in the various simulation runs whose snapshots were depicted in Fig. 2

4. Results

4.1. Scaling with r_p

As discussed in Ohtsuki (1993) in terms of 3-body integrations, the probability for pairwise gravitational sticking in impacts is determined solely in terms of (1) the strength of gravity via the r_p parameter, (2) the elasticity of impacts, and (3) the rms-impact velocity scaled to the mutual escape velocity. In low optical depth rings, the velocity dispersion, and thus also the rms-impact velocity, depends on the combined effects of mutual physical impacts and gravitational encounters, via the energy balance involving the collisional dissipation and the viscous gain of energy arising both due to impacts and gravitational forces (see, e.g., Stewart et al., 1984; Schmidt et al., 1999). When a constant coefficient of restitution is below its critical value ($\epsilon_{cr} = 0.627$ for $\tau \to 0$, Goldreich and Tremaine, 1978; Araki, 1991; Ohtsuki, 1999), the collisional viscous transfer of energy from the systematic velocity field will always maintain a minimum velocity dispersion of the order of $v_{imp} = kr\Omega$, where k is a numerical factor of the order of unity, its exact value depending on ϵ_n. The gravitational heating on the other hand tends to maintain a velocity dispersion of the order of escape velocity, $v_{esc} = \sqrt{2Gm/r}$ (see Salo, 1995, Fig. 15; Ohtsuki, 1999,

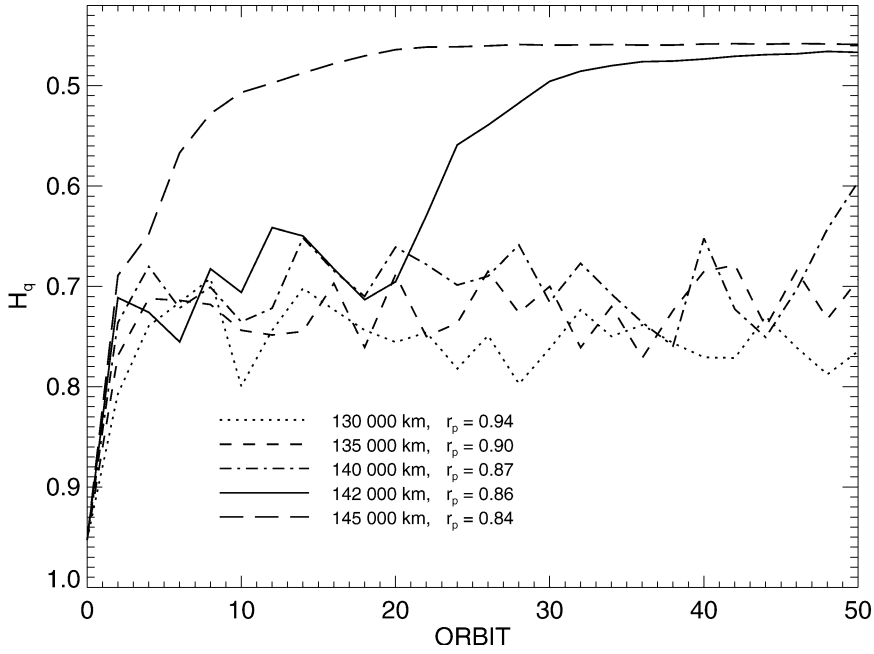

Fig. 5. Time evolution of Renyi entropy H_q in the simulation examples shown in Fig. 2. Parameters $q_H = 5$ and $m_x = m_y = 32$ were used.

Fig. 12). In terms of r_p parameter,

$$v_{imp}/v_{esc} = k(\epsilon_n)/\sqrt{24}\, r_p^{3/2}. \quad (26)$$

Thus the ratio of rms-impact velocities to the escape velocity will depend only on ϵ_n and r_p. In larger optical depths, the rms-impact velocities are affected also by the velocity disturbances connected to gravitational wakes, which according to Eq. (23) imply a velocity dispersion of the order of $v_{grav} \sim c_r = 3.36QG\Sigma/\Omega$ (mainly due to systematic motions between wakes; the local velocity dispersion inside the wakes may even remain close to escape velocity, see Section 4). For identical particles $\Sigma = m\tau/(\pi r^2)$, so that

$$v_{grav}/v_{esc} \approx 2.6Qr_p^{-3/2}\tau. \quad (27)$$

This introduces a possible optical depth dependence to sticking probabilities, but most importantly, no explicit dependence on the internal density or distance, besides that via the r_p parameter $\propto \frac{1}{\rho^{1/3}a}$. The same conclusion holds also in the case of size distribution. Thus, in the case of constant ϵ_n, the results of simulations performed with some specific internal density and distance can be readily scaled to any other value of ρ.

In the case of velocity-dependent ϵ_n, the dimensional scale parameter present in the elasticity law, like v_c in Eq. (19), complicates the situation, as the equilibrium velocity dispersion maintained by impacts will depend on both $r\Omega$ and v_c. In this case the v_{imp}/v_{esc} ratio may depend on the distance via $v_c/(r\Omega)$, besides r_p. Especially in the case of large v_c, corresponding to a slowly decreasing $\epsilon_n(v_n)$ relation, the steady-state velocity dispersion will scale proportional to v_c (Salo, 1991, 2001; Ohtsuki, 1999), whereas in the case of smaller v_c (rapid drop of elasticity with impact velocity), the steady-state is less sensitive to v_c. The former case corresponds to a multilayer steady-state while the latter one relates to a near mono-layer state. Thus at least in principle, separate runs would be needed to study the distance dependence of accretion for different ρ's. Nevertheless, for meter sized particles the steady-state behavior implied by the Bridges et al. elasticity law is very close to that for $\epsilon_n = \text{constant} \sim 0.5$, so that the expected effect is small. This is verified in Fig. 6, comparing the accretion versus r_p in two sets of runs, performed with $\rho = 450\ \text{kg m}^{-3}$ and $900\ \text{kg m}^{-3}$. In the former case, the particle radius and size of the calculation region have both been increased by a factor of two, to keep the optical depth and surface density unaltered (for identical particles $\tau = N\pi r^2/L^2$ and $\Sigma = 4/3\tau\rho r$). Because of the increased particle radius, the velocity dispersion due to impacts, scaled by $r\Omega$, is slightly reduced, leading to a somewhat easier gravitational sticking. However, the radial shift between the curves is not very significant, of the order of only one percent in r_p. For comparison, the figure also shows corresponding curves for $\epsilon_n = 0.5$, in which case the difference in curves follows just from statistical uncertainties.

In conclusion, the distances of accretion obtained for $\rho = 900\ \text{kg m}^{-3}$ can be safely scaled to any other internal density, also for a velocity-dependent ϵ_n according to Bridges et al. (1984) law, according to the formula

$$a_{acc}(\rho) = a_{acc}(900\ \text{kg m}^{-3})\left(\frac{\rho}{900\ \text{kg m}^{-3}}\right)^{-1/3}. \quad (28)$$

4.2. Independence of simulation parameters

Before looking at the effects of various physical parameters, we need to make sure that the results are not sensitive

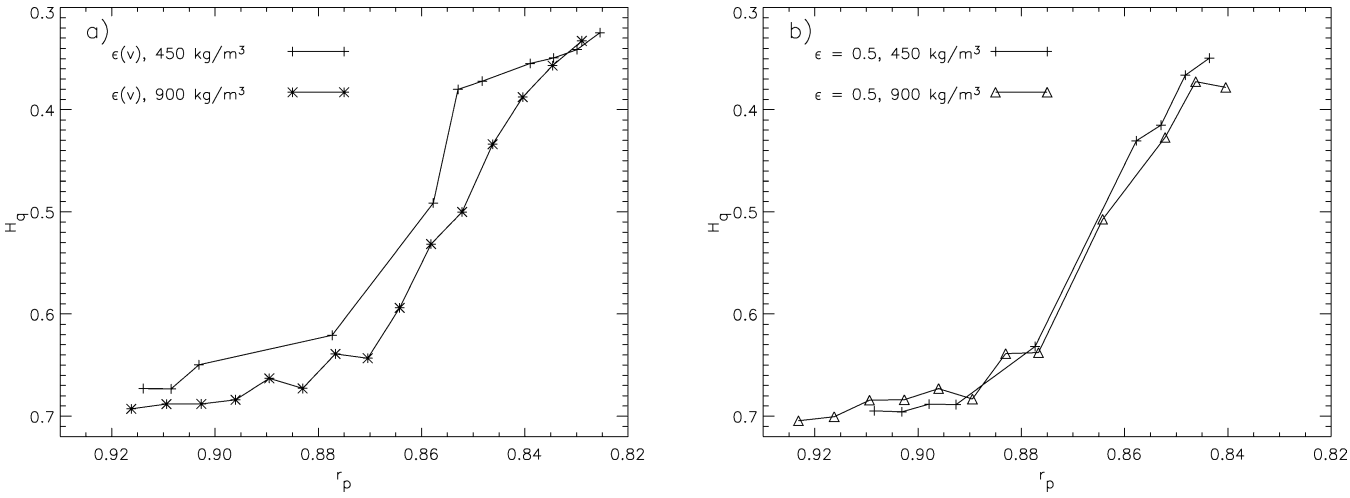

Fig. 6. Check of the accuracy of the r_p scaling with velocity-dependent coefficient of restitution. The curves at left compare H_q versus r_p parameter for the standard simulation case with Bridges et al. elasticity law and the internal density $\rho = 900\ \mathrm{kg\,m^{-3}}$, and a corresponding series except with $\rho = 450\ \mathrm{kg\,m^{-3}}$. Note that the r_p values correspond to different physical distances in these two simulation series, and the difference between curves comes from the additional distance dependence implied by the dimensional scale parameter in the Bridges et al. (1984) law. For comparison, the frame at right shows similar series for $\epsilon_n = 0.5$, the difference of curves now following solely from statistical uncertainties.

Table 1
Summary of accretion distances I: simulation parameter check[a]

	Accretion begins[b] (r_p)	Continuous accretion[b] (r_p)	Comment
ω_0/Ω			
3200	137,000 km (0.889)	143,000 km (0.852)	Fig. 7a
1600	135,000 km (0.903)	145,000 km (0.840)	
800	135,000 km (0.903)	145,000 km (0.840)	
400	137,000 km (0.889)	146,000 km (0.835)	
200	138,000 km (0.883)	146,000 km (0.835)	
100	139,000 km (0.877)	147,000 km (0.829)	
ΔT			
0.0010	137,000 km (0.889)	146,000 km (0.835)	Fig. 7b
0.0050	136,000 km (0.896)	145,000 km (0.840)	
N			
500	137,000 km (0.889)	146,000 km (0.835)	Figs. 7c–7d
1000	137,000 km (0.889)	145,000 km (0.840)	
2000	136,000 km (0.896)	143,000 km (0.852)	
5000	135,000 km (0.903)	142,000 km (0.858)	

[a] Based on visual detection of aggregates. Beginning of accretion corresponds to a distance where an aggregate was first obtained in at least one of the 20 simulations lasting 50 orbital periods. Continuous accretion refers to a distance where every simulation lead to an aggregate.

[b] Mass-ratio $m_1/m_2 = 1$ is used for the calculation of r_p in the parenthesis.

to simulation-method related parameters, the time step ΔT for the gravitational calculations, or the spring constant in the force model for impacts. Also, the number of particles used in the simulations might have an influence on the obtained accretion. These checks are done by using the standard model parameters introduced in Section 2, except for the studied parameter. Also, when varying the number of simulation particles N, the size of the simulation area is changed to keep the fixed optical depth $\tau = 0.25$. Results of these tests are shown in Fig. 7, and also in Table 1, summarizing the accretion distances based on the method 1 of Section 2.

4.2.1. Spring constant

Previous force model simulations (Salo, 1995; Salo et al., 2001) have indicated that the results (e.g., the steady-state velocity dispersion, the strength of gravity wake structures) are not sensitive to the adopted spring constant, as long as the impact duration is small compared to orbital timescale (say less than 0.01 orbital periods). In a non-gravitating case it is also easy to verify that the results are identical to those obtained by using instantaneous velocity changes in impacts. For longer impact durations, the actually obtained value of ϵ_n may start to deviate from that corresponding to a realistic short impact duration, due to the orbital motion during the impact, and due to the prolonged influence of gravity during the impact. Also, the maximal impact frequency is limited by the finite duration of the impact.

The restrictions for the allowable spring constant might be more severe in the present rather extreme case, focusing on the gravitational sticking of particles. In this case, the impact duration looses its meaning, a strong enough gravity leading to a situation where the particles can remain in contact after an impact, or a series of impacts, with a slight residual overlap in radius (this is different from the uncontrolled overlaps in the instantaneous impact method). This overlap amounts to (equating the harmonic impact force and the mutual gravity of a particle pair in contact),

$$\frac{\xi}{r + r'} \sim 3(\omega_0/\Omega)^{-2} r_p^{-3}, \tag{29}$$

and is thus completely negligible, concerning for example the volume density of a forming aggregate (note that in the center of a large aggregate with mass M_{clump} and diameter D_{clump}, the hydrostatic pressure will be proportional to

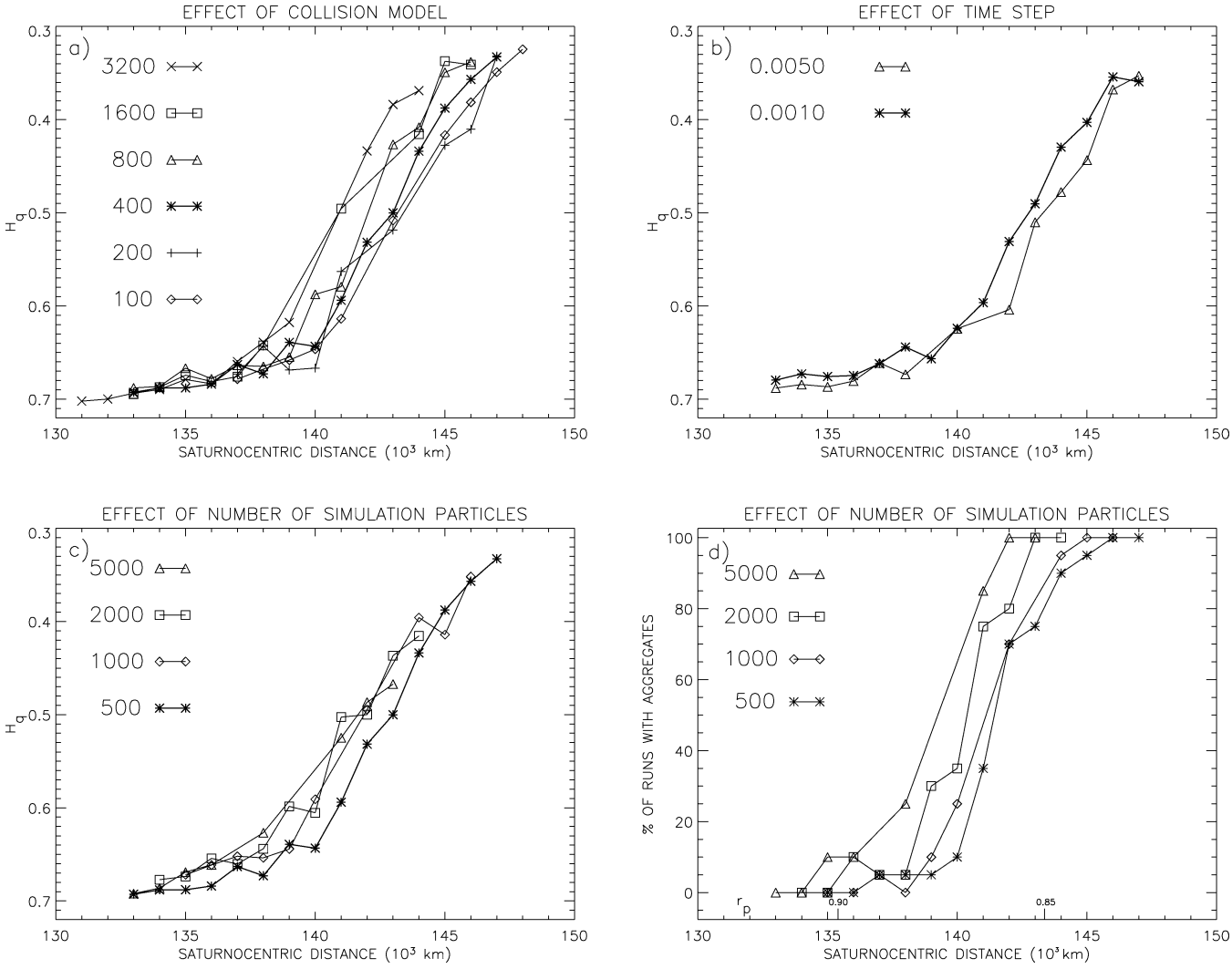

Fig. 7. Check of the effect of simulation-related parameters on accretion. In (a) different spring constants of force model are compared, labeled by the harmonic frequency, ω_0/Ω (in each case a different dissipation parameter, β in Eq. (14) was also applied, to give the same velocity-dependent ϵ_n). In (b) the effect of the gravity update interval, ΔT, measured in orbital periods. The improved gravity calculation method is used, Eq. (21). In (c) the effect of the number of simulation particles, shown in terms of Renyi entropy H_q, with the m, q_H scaling explained in the text: $q_H = 5, 6.5, 7.5$, and 9.0 for $N = 500, 1000, 2000$, and 5000, respectively. (d) Same as (c) with visual inspection, using the method 1 described in Section 2.

M^2_{clump}/D^4_{clump}, and a similar reasoning that leads to Eq. (29) indicates a residual overlap proportional to $(D_{clump}/r)^2$. This effect, however remains small for the number of particles we have used). Nevertheless, the particles are free to separate if a sufficient velocity impulse is provided by an impacting third particle. The stability of the forming aggregate against such external velocity impulses may depend on the force model parameters, since a smaller spring constant (longer impact duration) reduces the rate by which the aggregate can dissipate the injected energy.

For this reason, a wide range of spring constants was checked (Fig. 7a), extending from $\omega_0/\Omega = 100$ to 3200, the last value corresponding to an impact duration of the order of just 10 seconds, thus already approaching the physically realistic values. Although a small inward shift of the accretion boundary is seen when ω_0/Ω is increased, most likely due to the enhanced maximal dissipation, the overall effect is small: our standard $\omega_0/\Omega = 400$ can be expected to give correct distances for accretion with about 1% accuracy.

4.2.2. *Time interval of gravity updates*

With the improved gravity calculation method, Eq. (21), the results are not sensitive to ΔT (Fig. 7b). A small outward shift of accretion boundary is seen if a very long time step is used (0.005 orbital periods = 5 times our standard value), the difference being however less than 0.5%. Moreover, the results we obtain for the onset of accretion with the standard value $\Delta T = 0.001$ orbital periods are practically identical to those we obtained with the previous method, using constant forces during ΔT. However, with longer time scales the differences between methods become evident, related to the secular error of the previous method: the aggregates which are completely stable with the new method, continu-

Table 2
Summary of accretion distances II: effect of physical parameters[a]

	Accretion begins[b] (r_p)	Continuous accretion[b] (r_p)	Comment
ϵ_n			
0.1	127,000 km (0.960)	140,000 km (0.870)	Fig. 8a
0.5	136,000 km (0.896)	144,000 km (0.846)	
$\epsilon_n(v_n)$	137,000 km (0.889)	146,000 km (0.835)	
Friction			
no	137,000 km (0.889)	146,000 km (0.835)	Fig. 8b
0.01	137,000 km (0.889)	146,000 km (0.835)	
0.05	133,000 km (0.916)	140,000 km (0.870)	
0.1	129,000 km (0.945)	139,000 km (0.877)	
0.5	124,000 km (0.983)	133,000 km (0.916)	
Size distr.[c]	122,000 km (0.999) (0.692)[d]	134,000 km (0.909) (0.630)[d]	Fig. 9
τ			
0.05[e]	143,000 km (0.852)	151,000 km (0.807)	Fig. 10
0.10[e]	141,000 km (0.864)	147,000 km (0.829)	
0.25	137,000 km (0.889)	146,000 km (0.835)	
0.50	136,000 km (0.896)	142,000 km (0.858)	
0.75	136,000 km (0.896)	142,000 km (0.858)	

[a] Limiting distances determined as in Table 1.
[b] Mass-ratio $m_1/m_2 = 1$ is used for the calculation of r_p in the parenthesis.
[c] Lower and upper size limits are 0.5 and 5.0 m, respectively. The power-index for a power-law size distribution is $q = 3$.
[d] Mass-ratio $m_1/m_2 = 1000$ is used.
[e] These simulations lasted for 1000 orbital periods.

ously leak particles with the older method, due to a rotational instability (see Appendix A).

4.2.3. *Number of simulation particles*

The number of simulation particles N is crucial for the CPU time consumption, which scales $\propto N^2$ with the used method of direct particle–particle gravity. Therefore, it is desirable to be able to perform the survey with the value of N as small as possible, without biasing the results too much. Figures 7c and 7d compare runs with our standard parameters, except that N varies from 500 to 5000: since the comparison of H_q in runs with different N's is somewhat uncertain, also results from the visual detection method are shown. A small inward shift of accretion is visible for larger N's, most likely caused by the somewhat stronger wake structure with larger N, wakes acting as seeds for the aggregate formation. According to Salo (1995), a simulation region covering at least about $4\lambda_{cr}$ in the tangential direction, combined with $R_{grav} > 2\lambda_{cr}$, is needed to approximate the full strength of wakes. In the simulations of Fig. 7, $L/\lambda_{cr} \approx 1.7\sqrt{N/500}$, varying from 1.7 to 5.4 as N increases, leading to about 20% increase in the resulting Q parameter. Thus, although the wakes are present in our 500 particle experiments, their strength is underestimated in comparison to the actual strength the wakes should have. Another, though much less significant effect is due to the increased maximal mass ratio which can be obtained between an aggregate and an individual particle when N is increased. This reduces the aggregate-particle r_p parameter, promoting the sticking of new particles. However, this effect does not affect the initial pairwise sticking of particles, becoming significant only for aggregates containing nearly all the particles in the simulation. Altogether, the uncertainty caused on the accretion distances when using just 500 particles seems tolerable.

Table 3
Steady-state properties of identical particle simulations[a]

	c_{total} [cm s^{-1}]	c_{local} [cm s^{-1}]	c_{local}/v_{esc}	Q	L/λ_{cr}	Impacts/orbit
ϵ_n						
0.1	0.17	0.09	1.23	2.69	1.73	168
0.5	0.15	0.11	1.57	2.31	1.73	70
$\epsilon_n(v_n)$	0.14	0.10	1.46	2.27	1.73	58
k_f						
0.00	0.14	0.10	1.46	2.27	1.73	58
0.01	0.15	0.10	1.47	2.35	1.73	66
0.05	0.15	0.10	1.39	2.35	1.73	97
0.1	0.16	0.10	1.37	2.55	1.73	128
τ						
0.05	0.08	0.08	1.14	6.48	8.66	2.1
0.1	0.09	0.08	1.16	3.38	4.33	5.3
0.25	0.14	0.10	1.46	2.27[b]	1.73	58
0.5	0.22	0.12	1.64	1.69[b]	0.87	251
0.75	0.30	0.13	1.78	1.57[b]	0.75	405

[a] Quantities characterizing the steady-state properties of the simulation systems of Section 4.3, at a fixed distance $a = 130{,}000$ km, just inside the region where accretion starts.
[b] The reduction of Q with τ in these simulations is due to reduced size of the simulation system measured in terms of L/λ_{cr}.

4.3. *Dependence of accretion on physical quantities*

In this section we study the influence of various physical quantities on the distances where accretion is expected. The summary of accretion distances for different physical parameters are shown in Table 2. In addition, Table 3 lists the velocity dispersions and impact frequencies in these experiments, for a common distance $a = 130{,}000$ km, characterizing the steady-state properties in the region just inside the distances where significant accretion begins. Both local (c_{local}) and total (c_{total}) velocity dispersion are listed: the former is calculated from the relative velocities of neighboring particles (using 10 nearest neighbors; see Salo, 1995). Note that the local dispersion is more relevant for the pairwise gravitational sticking than the total dispersion, which includes also the systematic motions between the wakes.

4.3.1. *Coefficient of restitution*

In Fig. 8a, a velocity-dependent coefficient of restitution is compared to two different constant values of ϵ_n. Using $\epsilon_n = 0.5$ gives very similar results with $\epsilon_n(v_n)$, as was already indicated in Fig. 6. However, with the smaller elasticity, $\epsilon_n = 0.1$, accretion occurs almost 10% closer to the

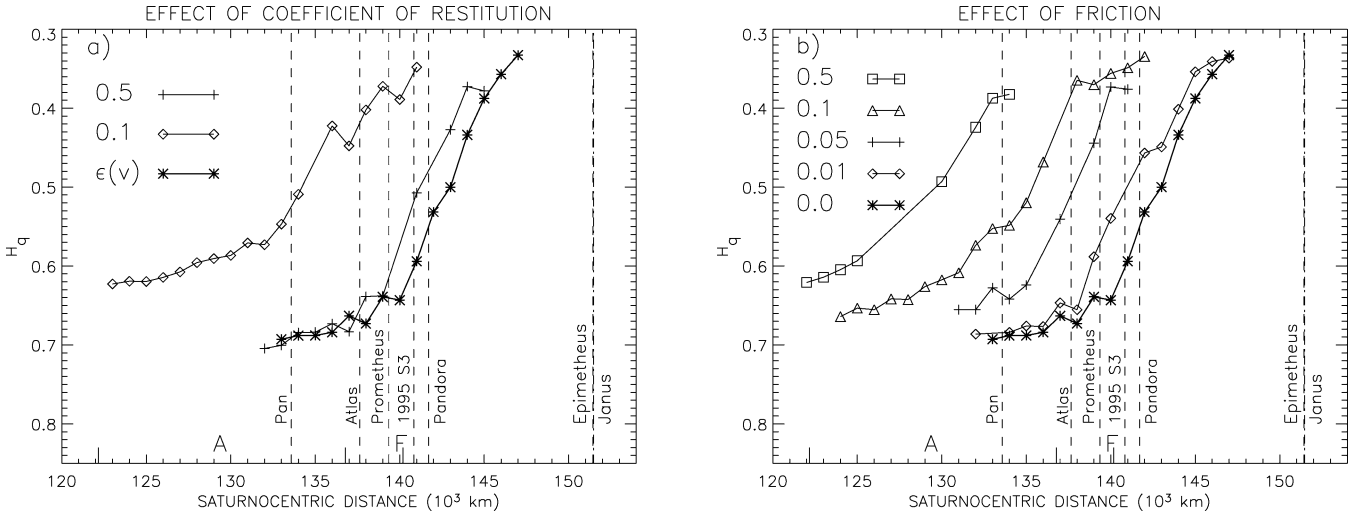

Fig. 8. In (a) velocity-dependent coefficient of restitution is compared to different constant values of restitution. In (b) different values for the coefficient of friction k_f are compared, for the standard velocity-dependent ϵ_n model. In both cases accretion is measured with H_q.

planet. This enhanced accretion is caused by several factors. First of all, for fixed r_p and velocity dispersion, the sticking probability increases rapidly when ϵ_n is reduced (Ohtsuki, 1993). In addition, stronger dissipation promotes the formation of gravitational wake structures, providing seeds for aggregate formation. In Table 3 the stronger wake structure is evidenced by the higher Q values (calculated by using total velocity dispersion c_{total}) for $\epsilon_n = 0.1$; for the same reason the H_q levels for small a's in Fig. 8a are smaller for $\epsilon_n = 0.1$ than for $\epsilon_n = 0.5$. Simultaneously c_{local} becomes smaller for smaller ϵ_n. Also impact frequency is enhanced, by about a factor of two between $\epsilon_n = 0.1$ and 0.5, speeding up the formation of aggregates.

4.3.2. Friction between the colliding particles

Since friction enhances the collisional dissipation, essential for particle sticking, it is not surprising that its inclusion leads to accretion at smaller distances, in a similar fashion as reducing ϵ_n. In Fig. 8b, a fairly large range of k_f is studied, due to the large inherent uncertainty in its actual value. In the case of weak friction (say $k_f = 0.01$) its effect is fairly marginal. However, if for some reason the actual friction is more effective, say $k_f = 0.1$, an inward shift of several thousands of kilometers can be expected.

A crude estimate can be made concerning the relation between the role of reduced ϵ_n and a non-zero friction. The energy dissipation in impacts is proportional to (e.g., Hämeen-Anttila and Salo, 1993),

$$\Delta E_{diss} \propto \frac{1}{2}\left(1-\epsilon_n^2\right)\langle v_n^2\rangle + \frac{1}{7}\left(1-\epsilon_t^2\right)\langle v_t^2\rangle, \tag{30}$$

where v_n and v_t denote the perpendicular and tangential components of the impact velocity and the pre-factor of the latter term differs from that of the first term since particle spins are taken into account. In the case of random impact directions, and ignoring the small spin contribution in Eq. (17), we can approximate $\langle v_n^2\rangle = \langle v_t^2\rangle$ (averages are weighted according to probability of impact, proportional to $|v_n|$). Equation (30) can then be used to define an approximative effective value of ϵ_{eff}, which in the absence of friction would yield the same energy dissipation/impact as the actual ϵ_n, ϵ_t values, by

$$\left(1-\epsilon_{eff}^2\right) = \left(1-\epsilon_n^2\right) + \frac{2}{7}\left(1-\epsilon_t^2\right). \tag{31}$$

Thus for example if $\epsilon_n = 0.5$ and $\epsilon_t = 0.4$, this would imply $\epsilon_{eff} \approx 0.1$. According to Eq. (20), for $\epsilon_n = 0.5$, the value $k_f = 0.1$ corresponds roughly to $\epsilon_t = 0.4$, provided that typical $v_t \sim v_n$. Indeed, comparison of the curve for $k_f = 0.1$ in Fig. 8b and the curve for $\epsilon_n = 0.1$ in Fig. 8a indicates this rough estimate to be at least approximately valid.

4.3.3. Size distribution

The influence of including the particle size distribution is very clear, as can be anticipated based on Eq. (6). Compared to the standard model with identical particles, our size distribution with maximal mass ratio of 1000 leads to an almost 10,000 km inward shift in the accretion boundary (Fig. 9), in agreement with the few examples given in Salo (1995). In terms of the r_p parameter for identical particles, the shift in accretion distance corresponds to $r_p = 0.83 \rightarrow 0.91$. Nevertheless, this shift is not nearly as strong as could be expected based on the difference in the r_p parameter calculated for the maximal mass ratio $\mu = 1000$ and for identical particles (they would differ by a factor of 0.7, see Section 2). This might indicate that the reduced r_p value for the smallest/largest particle pair is not the crucial factor, the overall accretion depending perhaps more on the evolution of intermediate mass ranges. Another important factor, reducing the sticking efficiency of the smallest particles to the surfaces of the largest ones is the increased velocity dispersion of the small particles. In fact, according to Table 3, v_{imp}/v_{esc} is smallest for the mutual impacts between the largest particles themselves. Indeed, an inspection of simulation snap-

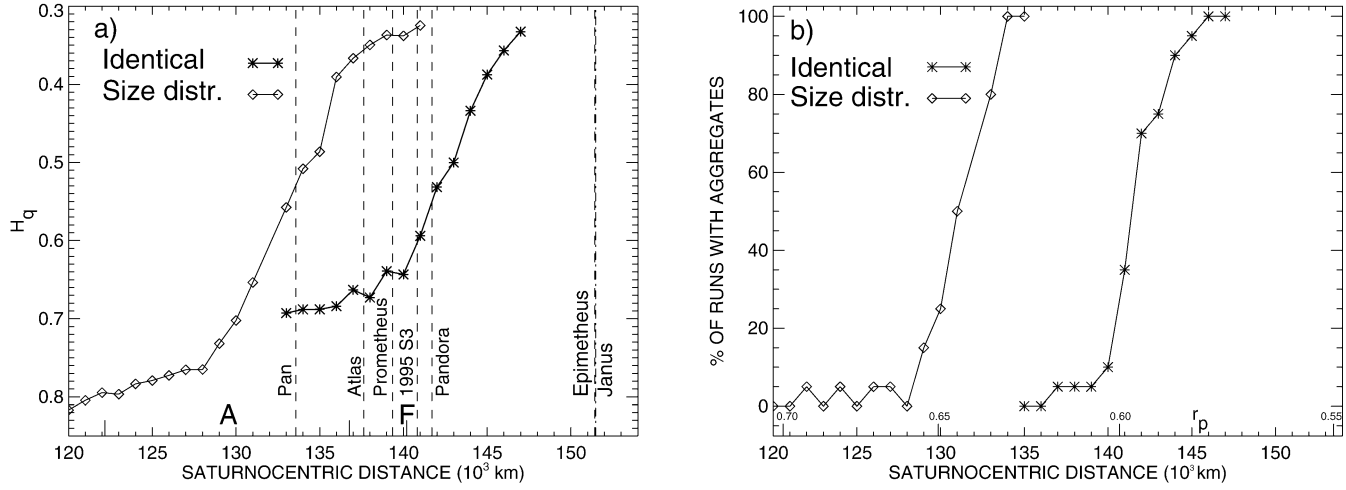

Fig. 9. *Size distribution*. Simulations with a power law size distribution are compared to the standard case of identical particles. In (a) accretion is measured with H_q while in (b) visual detection is used. Since H_q measures inhomogeneities in the number density distribution, it is not well suited for case with large differences in the masses of individual particles. Still, results for accretion when using H_q and visual inspection are fairly similar.

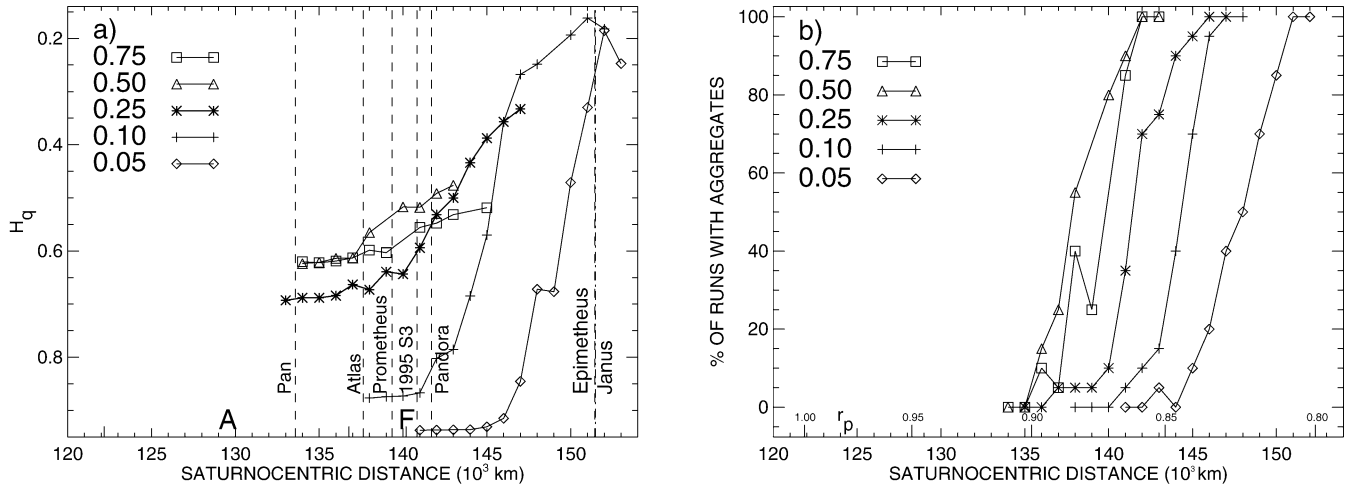

Fig. 10. *Optical depth*. Five different optical depths are compared, $\tau = 0.05, 0.10, 0.25, 0.50$, and 0.75 corresponding to surface density $\Sigma = 60, 120, 300, 600$, and 900 kg m^{-2}, respectively. Simulations for the optical depths 0.05 and 0.10 were extended to 1000 orbital revolutions to account for the expected longer accretion timescale due to reduced impact frequency. In (a) accretion is measured with H_q while in (b) visual detection is used. The scaled values for q_H were 2, 3.5, 5.0, 8.0, and 13, in the order of increasing τ.

shots indicates that the particle aggregates seem to initiate mainly via grouping of big particles, subsequently collecting smaller ones.

4.3.4. Optical depth

The optical depth at the outer parts of Saturn's A ring is about 0.5–0.6, which is higher than in our standard model with $\tau = 0.25$. Thus, larger values of $\tau = 0.5$ and $\tau = 0.75$ were also studied (Fig. 10). Increasing τ from 0.25 to 0.50 makes the accretion more efficient, probably because there are stronger wakes present (as indicated by the increased total velocity dispersion in Table 4, and the smaller H_q values in the non-accretion region, see Fig. 10a). Interestingly, increasing τ even more, to 0.75, has a slight opposite effect (this is not an artifact of H_q scaling, being also marginally visible in Fig. 10b, displaying the fraction of simulations leading to accretion), suggesting that the accretion tendency might also be suppressed due to crowding of particles in wakes, indicating frequent impacts between the seed aggregates.

In addition, also smaller optical depths, $\tau = 0.1$ and 0.05 were studied, in which case no wakes are present. The region of accretion is seen to move significantly outward. Nevertheless, this could be largely due to the methods we use for measuring accretion, which are all sensitive to the timescale of accretion, if this becomes comparable to the length of the simulation. To reduce this bias, the simulations of low τ were continued for 1000 orbital periods instead of 50 orbits. On the other hand, the accretion at low τ might be genuinely more inefficient as in the absence of wakes the accretion must start and proceed in a pairwise fashion, via collisions of individual particles and/or the formed small-N

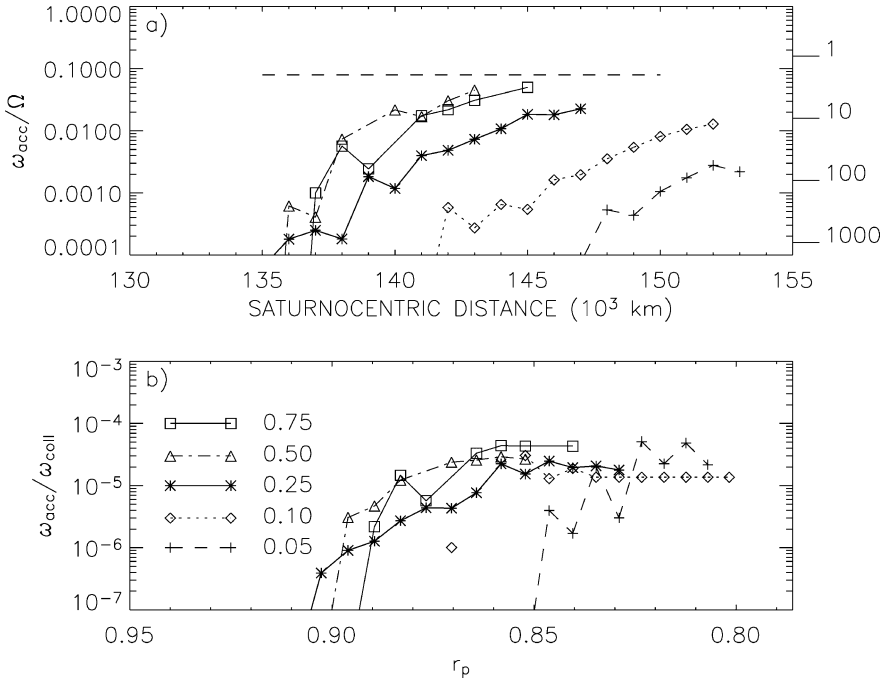

Fig. 11. *Timescales of accretion.* In (a) the accretion frequency, in units of orbital frequency, is compared for different optical depths (see text for details). The accretion time scale is indicated in the right-hand axis, in units of orbital periods. Dashed line indicates the upper limit for the obtained accretion frequency, imposed by our sampling of snapshots every 2 orbital periods. In (b) the accretion frequency is measured with respect to impact frequency: the inverse of this indicates the average number of impacts/particle before accretion has occurred in the simulation.

aggregates. Impacts between such small rubble piles might be on the average more destructive than impacts with the already fairly large clumps forming inside the wakes in the large τ case, simply because the effective volume filling factor of the irregular small-N clumps is smaller than that of the larger, nearly spherical aggregates. Due to the same reason they are also more fragile against spontaneous tidal disruption.

Figure 11 studies the time scale of accretion, in terms of the average duration required for an aggregate to form. The frequency of aggregate formation is defined by

$$\omega_{\rm acc} = \left\langle \frac{1}{T_{\rm acc}} \right\rangle, \tag{32}$$

where $T_{\rm acc}$ is time from the beginning of the simulation to the instant when an aggregate is first observed; this is set to infinity if no aggregate forms at all. Since 20 runs are employed in taking the average for each distance and τ, the obtained $\omega_{\rm acc}$ may be smaller than $1/T_{\rm max}$, where $T_{\rm max}$ is the maximum duration of the single run; in any case $\omega_{\rm acc}$ is then very uncertain. The $\omega_{\rm acc}$ is also limited from above to $\frac{1}{2} \times \frac{\Omega}{2\pi}$, since snapshots taken only every two orbital periods are studied. This is not a serious restriction, because very rapid accretion rates would in any case be uncertain, being affected by the initial velocity dispersion of the system, before the system has time to achieve a steady-state. Figure 11a, displaying $\omega_{\rm acc}$ versus distance, shows how the accretion frequency drops rapidly for smaller τ's. Mainly this is due to a reduced impact frequency for smaller τ,

Table 4
Steady-state properties of particle simulations with size distribution at $a = 130,000$ km[a]

	$\langle r \rangle$	N	$c_{\rm total}$ [cm s^{-1}]	$c_{\rm local}$ [cm s^{-1}]
Small	0.68	395	0.48	0.41
Intermediate	1.47	85	0.35	0.29
Large	3.21	19	0.26	0.22
	$v_{\rm imp}$	$v_{\rm esc}$	Impacts/orbit	
Small–small	0.24	0.05	50/small particle	
Small–large	0.20	0.21	110/large particle 5/small particle	
Large–large	0.11	0.23	150/large particle	

[a] The simulation system with $r_{\rm min} = 0.5$ m, $r_{\rm max} = 5$ m, $q = 3$, was divided into 3 logarithmic size bins (small, intermediate and large), for which the average velocities were calculated. Average rms-impact velocities between selected size groups are also shown.

studied more quantitatively in Fig. 11b. Here the accretion frequency is shown scaled to impact frequency, calculated from the average number of impacts per particle, $N_{\rm acc}$, before the first aggregate has formed,

$$\omega_{\rm acc}/\omega_{\rm coll} = \left\langle \frac{1}{N_{\rm acc}} \right\rangle. \tag{33}$$

This scaling reduces the shift between the curves for different τ's, but it still seems that a larger number of impacts might be required in the low τ case before accretion, emphasizing the role of wakes in speeding up the accretion process in comparison to just pairwise sticking.

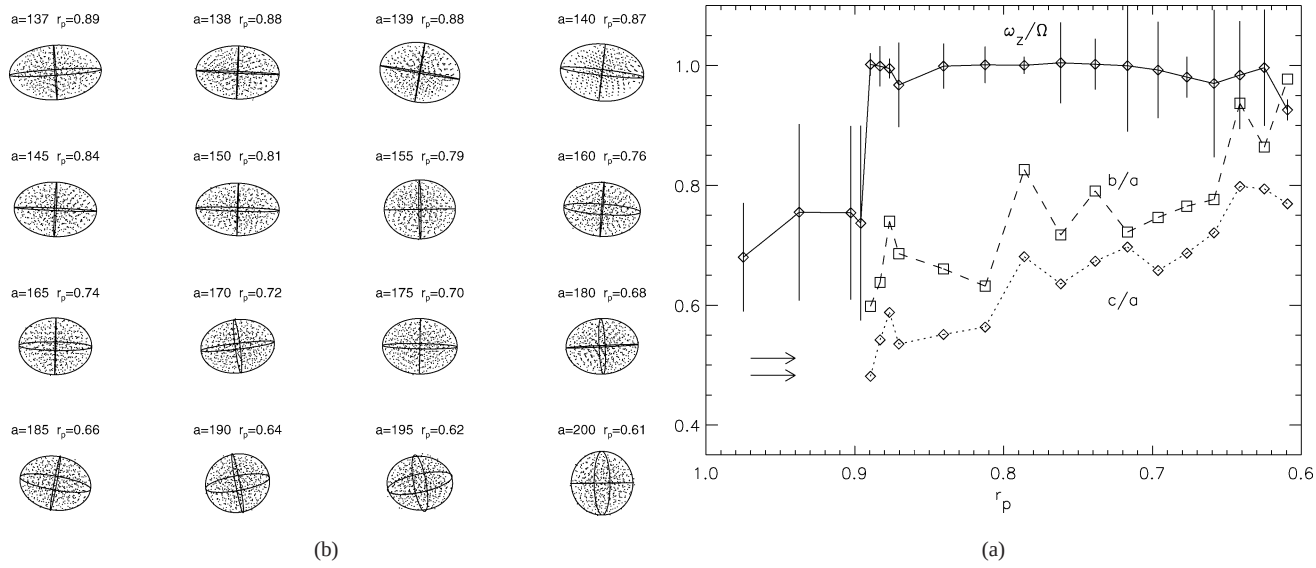

Fig. 12. *Rotation and shape of aggregates*. In (a) examples of aggregates formed at different distances ($a = 137{,}000$–$200{,}000$ km). The standard simulation case, except with $k_f = 0.1$ was studied: in each case all 500 particles had accumulated into a single aggregate. The projections of the particle distributions to the equatorial plane are shown after 100 orbital periods, together with a fitted 3-axial ellipsoid, corresponding to a homogeneous body with the same principal axis values of the mass tensor as for the simulated aggregate. Note that in each case the longest principal axis $\hat{a}$ is nearly radially aligned, and the shortest axis $\hat{c}$ ($\sim$ spin axis) is close to being perpendicular to the equatorial plane. Note however that the deviation of $\hat{c}$ from perpendicular direction tend to increase for larger distances ($r_p < 0.7$). All aggregates are shown in the same scale: their typical long axis are 20–30 m. In (b) the vertical component of the mean spin of the particles (corresponds to the spin of the aggregate for $a \gtrsim 137{,}000$ km), and the principal axis ratios b/a and c/a are shown as a function of r_p parameter. Error bars denote standard deviation which are calculated from the last 10 orbits. Aggregate at distance 200,000 km is also in synchronous rotation but its rotational axis is tilted. Arrows indicate the axial ratios for the most elongated stable Roche ellipsoid with $b/a = 0.511$, $c/a = 0.483$ (see Chandrasekhar, 1969).

4.4. Rotation and shape of aggregates

A brief study of the rotation and shape of the forming aggregates was also made, using simulations where friction was included, with $k_f = 0.1$ (Fig. 12). The inclusion of friction and particle spins makes it easy to measure the aggregate rotation, since when an aggregate forms, the relative velocities between its particles are rapidly damped, the aggregate behaving almost like a rigid body: thus its rotational state is readily obtained from the mean spin of its constituting particles. In the case displayed in Fig. 12, the aggregate formation starts beyond $a = 137{,}000$ km. Slightly inside this distance, the mean spin of particles has a non-zero vertical component, amounting to $\omega_z/\Omega \sim 0.6$, being about twice as large as in the case of non-gravitating particles, in agreement with the single experiment in Salo (1995). The rotational state of the eventually formed aggregates is found to be almost exactly synchronous. Depending on the initial formation history, however, some decaying oscillations around the exact radial alignment may be present even in the end of the simulations (100 orbital periods).

As can be expected, the shape of the aggregates has a general tendency of becoming more spherical for larger distances when the tidal effects diminish in comparison to self-gravity. In addition, near the inner limit where aggregates are first obtained, their shape is rather close to that of the Roche-ellipsoids: the arrows in Fig. 12 indicate the extreme axial ratios of the last stable Roche ellipsoid as the distance to the planet is reduced (see, Chandrasekhar, 1969, p. 189). However, in individual simulations large deviation from this trend are visible (Fig. 12b). Most likely this scatter reflects the sensitivity of the shape to the exact formation history: the shape of the clumps forming via gradual accretion of single particles is likely to reflect the tidal environment better than aggregates formed via a coalescence of several clumps, tending to retain a memory of their initial more or less random shape throughout the simulation.

In each of the small N examples displayed in Fig. 12a, only one aggregate survived to the end of the simulation, all initial clumps rapidly merging into a single body. However, with larger N several aggregates can form in the simulation region (see, e.g., Fig. 2), and if these are separated by large enough radial distances, they can stay stable throughout the simulation (note however that our limiting distance R_{grav} for gravitational calculations makes this somewhat easier than in reality). In a few simulations also aggregates with a strong temporary retrograde rotation were observed: inspection of the initial evolution showed that these aggregates formed via a coalescence of two almost equal sized initial clumps, having a favorable impact angular momentum. However, during the course of the simulation also these initially retrograde clumps gradually evolved toward synchronous rotation.

5. Discussion and summary

We have performed a simulation survey of the onset of aggregate formation in Saturn's rings, via local N-body sim-

ulations including mutual impacts and gravitational forces between particles. Various methods for detection of accretion in simulations were compared, suggesting that the calculation of Renyi entropy provides one possible, easily automatized method, giving results which agree with those from the much more tedious visual inspection of simulation snapshots. Various simulation method related parameters were checked, including those related to the used force method for the calculation of impacts, as well as factors related to the calculation of self-gravity. In particular, we showed that a potential pitfall exist in our previous calculation method of self-gravity (Salo, 1995), which works adequately in the case of gravity wakes, but leads to artificial rotational instability when long term aggregate evolution is followed. A simple improvement was devised, completely avoiding this problem while remaining computationally efficient.

The performed survey indicates that for 1-meter sized identical particles with solid ice density $\rho = 900\ \mathrm{kg\,m^{-3}}$, and Bridges et al. type velocity-dependent elasticity $\epsilon_\mathrm{n}(v_\mathrm{n})$, the particle groups start forming at distance $a = 136{,}000$ km, when the optical depth is close to the A ring value. Typically, the transition from non-accretion to accretion takes place over a relatively wide transition zone: only beyond 145,000 km, corresponding to $r_\mathrm{p} \approx 0.84$, are stable groups seen in practically all separate experiments. For a constant $\epsilon_\mathrm{n} = 0.5$ the behavior is about the same as with $\epsilon_\mathrm{n}(v_\mathrm{n})$, whereas for $\epsilon_\mathrm{n} = 0.1$ the accretion is moved closer to planet by almost 10,000 km (perfect accretion takes place for $r_\mathrm{p} < 0.87$). Inward shift is also obtained when friction is included to the impact model. In the case of power-law size distribution the transition to aggregate formation moves also significantly inward, about 8000 km in comparison to identical particles (for $q = 3$, and $0.5\ \mathrm{m} < r < 5\ \mathrm{m}$). For different internal densities these distances scale with $(\rho/900\ \mathrm{kg\,m^{-3}})^{-1/3}$. In the case of moderately large τ the aggregate formation seems to initiate via clumping of wakes, in a very short time scale ~ 10 orbital periods, whereas for low τ the time scale for accretion increases, mainly due to reduced impact frequency. The final rotational state of the found aggregates is always very near to synchronous rotation.

In Saturn's rings one can find microscopic dust, macroscopic ring particles, wakes, clumps, moonlets and moons. In principle, the outer edge of the Saturn's main ring at $a = 136{,}800$ km could be interpreted as the distance beyond which a ring of discrete particles would eventually accrete into larger bodies or moonlets. Interestingly, the standard model with solid ice density, the Bridges et al. (1984) coefficient of restitution, combined with the size distribution, leads to the onset of strong accretion at nearly this distance. Clearly this interpretation is not without difficulties, as evidenced by the existence of the F ring outside the A ring, as well by the presence of the satellite Pan in the Encke gap. Also, there are several factors not addressed in our models, like the effects of satellite resonances, or the possible significance of surface adhesion of particles. Also, the simulations a rather crude, having a limited number of particles and limited timescale. Thus, although we have indicated the expected effect of the main physical parameters (factors like internal density and friction besides the ϵ_n and size distribution), drawing any firm conclusions on their exact values is difficult.

Already inside the region of excessive aggregate formation a substantial amount of temporary particle groupings is predicted by the simulations. Indeed, there are evidence for an increased maximum size of particles in the A ring (Showalter and Nicholson, 1990; French and Nicholson, 2000). On the other hand, the A ring azimuthal brightness asymmetry, which seems to be naturally accounted by the presence of gravity wakes (Salo and Karjalainen, 1999; Porco et al., 2001; Salo et al., 2004), also sets constraints for the maximal strength of accretion: the peak of the asymmetry amplitude near 130,000 km is difficult to explain if the wakes are already very clumpy in this distance (Salo and Karjalainen, 1999), since the strong longitude dependence would then be significantly diluted. Clearly, more studies of the photometric consequences of possible particle aggregates are required, for example with the methods used in Salo and Karjalainen (2003).

If we assume that significant accretion occurs continuously inside the main rings what is then the factor that limits the aggregate growth and maintains the bulk of the power law size distribution? For a fixed internal density of an aggregate, the strength of its self-gravity scales proportional to its radius, in exactly the same fashion as the disrupting tidal and rotational stresses for a nearly synchronously rotating body. In fact, there are factors which could even promote a more efficient growth of bigger aggregates: for example the elasticity of impacts is likely to decrease with the larger impact speeds implied by the increased escape velocity of a growing moonlet. A possible limiting factor is the reduction in the effective density of the growing moonlet, but at least so far numerical simulations have not given any evidence for this. Nevertheless, to ascertain this, simulation with several orders of larger N's should be performed. Another regulating factor could be the mutual impacts of aggregates. And if anything else fails, the moonlet will eventually clear a gap preventing, or at least significantly slowing down any subsequent growth (Sremčević et al., 2002).

In the present simulations we have focused just on the onset of aggregate formation. Mainly this is due to the restriction of the present method: the fixed number of particles and the applied strictly periodic boundary conditions. Because of the latter ingredient, the free particles surrounding the moonlet are always strongly perturbed by its gravity, even when leaving and re-entering the calculation region. In order to follow in a realistic manner the subsequent growth of the aggregate, the evolution of its volume filling factor, rotation and shape, a continuous flow of fresh ring particles would be required, the distribution of these particle orbits representing the ring regions not yet perturbed by the aggre-

gate. Also the effects of mutual impacts between aggregates should be studied. Eventually, the most feasible method to address the accretion and its effects on particle size distribution is via incorporation of numerical results into analytical or semi-analytical studies, like those by Longaretti (1989) and Barbara and Esposito (2002). Work on this direction will be reported in future studies.

Acknowledgments

This work was supported by the Academy of Finland and the Väisälä Foundation. We thank Pierre-Yves Longaretti and Keiji Ohtsuki for their detailed and helpful reviews.

Appendix A. Approximative treatment of self-gravity

Major part of the CPU consumption in simulations is due to the calculation of self-gravity. The approximation where self-gravity is updated less frequently than the impact forces is thus essential, speeding up the code even by a factor of ~ 100, as compared to the case where self-gravity were calculated at every RK4 step. Earlier simulations (Salo, 1995) have indicated that gravity update intervals $\Delta T \sim 0.005$ orbital periods already yield a sufficient accuracy for calculations dealing with the formation of wake structures. Nevertheless, the use of constant forces during ΔT has potential pitfalls, becoming evident when longterm evolution of particle aggregates is studied. This results from a secular increase of the energy of the particles forming the aggregate, leading to its eventual rotational instability. The timescale of this instability is inversely proportional to ΔT, so that a reduction of ΔT is insufficient to remove this problem. However, in this appendix we show how a very simple modification, with insignificant CPU overhead, cures the instability, the remaining secular energy input terms being proportional to ΔT^3.

In the absence of mutual impact forces, or boundary crossings, the linearized equations (7)–(9) possess an energy integral,

$$E = \sum_i^N m_i \left(\frac{1}{2} {V_i}^2 - \frac{3}{2} \Omega^2 {x_i}^2 + \frac{1}{2} \Omega^2 {z_i}^2 \right) - \frac{1}{2} \sum_{\substack{j=1 \\ j \neq i}}^N \frac{G m_i m_j}{r_{ij}}, \tag{A.1}$$

where $V_i = \dot{x}_i^2 + \dot{y}_i^2 + \dot{z}_i^2$. Partially inelastic impacts reduce the total energy, but in the steady-state this dissipation is balanced by the energy input via the periodic radial boundaries, corresponding to the viscous gain of energy. The approximative calculation of gravity amounts to an extra energy change with rate

$$\Delta \dot{E} = \sum_i^N \vec{V}_i \cdot \Delta \vec{F}_i, \tag{A.2}$$

where $\Delta \vec{F}_i = \vec{F}_i - \vec{F}_i^*$ is the deviation between the true gravity force $\vec{F}_i$ and that used in the approximative calculation, $\vec{F}_i^*$. Now the force $\vec{F}_i$ can be expanded to a Taylor series at the time t_0 (see Aarseth, 1972),

$$\vec{F}_i(t) = \vec{F}_i(t_0) + \dot{\vec{F}}_i (t - t_0) + \frac{1}{2} \ddot{\vec{F}}_i (t - t_0)^2 \cdots, \quad (t - t_0) < \Delta T, \tag{A.3}$$

with

$$\vec{F}_i = \sum_{\substack{j=1 \\ j \neq i}}^N -G m_i m_j \frac{R_{ij}}{r_{ij}^3}, \tag{A.4}$$

$$\dot{\vec{F}}_i = \sum_{\substack{j=1 \\ j \neq i}}^N -\frac{G m_i m_j}{r_{ij}^3} \left(\vec{V}_{ij} - 3 (\vec{R}_{ij} \cdot \vec{V}_{ij}) r_{ij}^{-2} \vec{R}_{ij} \right), \tag{A.5}$$

$$\ddot{\vec{F}}_i = \sum_{\substack{j=1 \\ j \neq i}}^N -\frac{G m_i m_j}{r_{ij}^3} \times \left[\vec{A}_{ij} - 6 (\vec{V}_{ij} \cdot \vec{R}_{ij}) r_{ij}^{-2} \vec{V}_{ij} + \left[-3 \left(v_{ij}^2 + \vec{R}_{ij} \cdot \vec{A}_{ij} \right) r_{ij}^{-2} + 15 (\vec{R}_{ij} \cdot \vec{V}_{ij})^2 r_{ij}^{-4} \right] \vec{R}_{ij} \right], \tag{A.6}$$

where $\vec{R}_{ij}$ and $\vec{V}_{ij}$ denote the relative position and velocity of particle j with respect to particle i at the time t_0, $r_{ij} = |\vec{R}_{ij}|$ and $v_{ij} = |\vec{V}_{ij}|$. The $\vec{A}_{ij}$'s represent the relative accelerations, taking into account both the central field and self-gravity at time t_0.

In the case constant forces are used during ΔT, the leading term in $\Delta F_i = -\dot{\vec{F}}_i (t - t_0)$. Averaged over the interval ΔT, the corresponding energy error (in principle, $\vec{V}_{ij}$ needs also be expanded as a Taylor series around $t = t_0$, but this does not contribute to the leading term in the error)

$$\Delta \dot{E}_1 = \frac{1}{4} \Delta T \sum_{\substack{j=1 \\ j \neq i}}^N \frac{G m_i m_j}{r_{ij}^3} \times \left[v_{ij}^2 - 3 (\vec{V}_{ij} \cdot \vec{R}_{ij})^2 r_{ij}^{-2} \right]. \tag{A.7}$$

In the case $\vec{V}_{ij}$ and $\vec{R}_{ij}$ are not strongly correlated, this error vanishes since $\langle v_{ij}^2 \rangle \approx 3 \langle (\vec{V}_{ij} \cdot \vec{R}_{ij})^2 r_{ij}^{-2} \rangle$. Although this is not strictly true in any actual wake simulation, the error averaged over all particle pairs is small in comparison to the dissipative and viscous energy changes, and is thus accommodated by a slight modification of the steady-state. However, the situation changes completely when an aggregate has formed. If the aggregate is treated as a single spherical particle, labeled with the index j, all the particles i in its surface have $\vec{V}_{ij} \cdot \vec{R}_{ij} \approx 0$. Thus, $\Delta \dot{E}_1$ is always positive. Since the shape of the aggregate is more or less rigid, its energy dissipation rate is typically very small (or it can vanish altogether) in comparison to $\Delta \dot{E}_1$, indicating a secular increase in its energy. In practice this energy increase manifests as growing oscillations around its initially radially

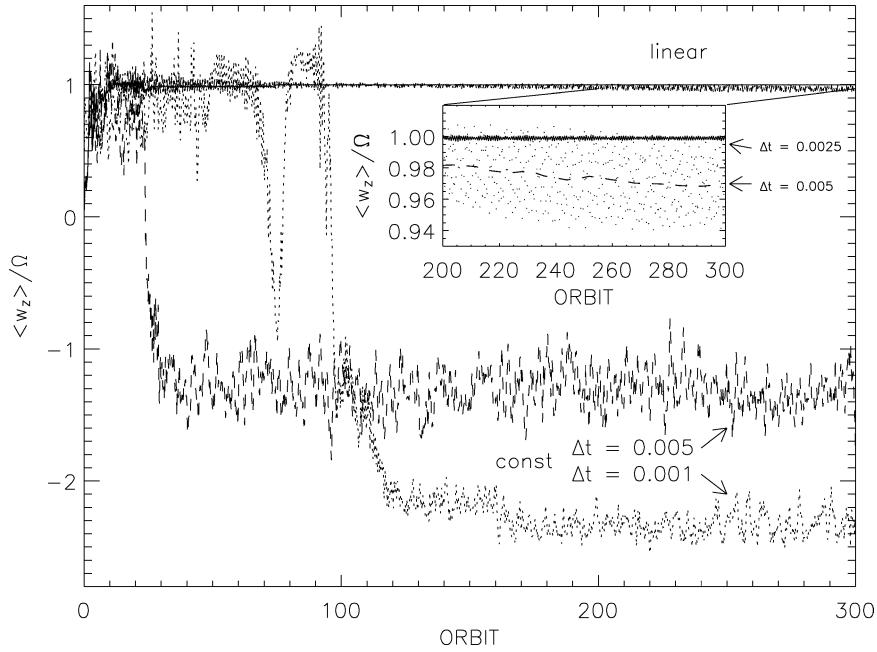

Fig. 13. Comparison of gravity calculation methods, using both a constant gravity during the time interval ΔT (curves labeled by "const"), and by using a linear expansion of force during ΔT ("linear"). The simulations correspond to the standard case for $a = 140,000$ km, except that friction is included, $k_f = 0.1$. The vertical component of the mean spin, normalized to the orbital frequency is shown: in these runs practically all simulation particles collect into a single aggregate during the first tens of orbital periods: the $\langle\omega_z\rangle/\Omega$ thus equals the spin of the aggregate. In the case of using constant forces, results for $\Delta T = 0.001$ and 0.005 are compared, indicating how the aggregate first rapidly approaches a nearly synchronous rotation state, however with large, growing oscillations, finally stabilizing itself in a state of retrograde rotation. For shorter ΔT the timescale for this artificial instability is prolonged, roughly proportional to $1/\Delta T$. On the other hand, when using the linear force expansion, the aggregate remains in a synchronous rotation: a small secular inaccuracy is seen with a longer time step ($\Delta T = 0.005$; see the insert, where the dashed line indicates the time average of $\langle\omega_z\rangle/\Omega$ for $\Delta T = 0.005$, calculated from the instantaneous values shown by points), but this tendency is not visible when $\Delta T = 0.0025$ (the solid line in the insert).

aligned orientation. When these oscillations reach a large enough amplitude, the tumbling of the aggregate becomes chaotic, and simultaneously particles start to leak from its surface. Curiously enough, an apparently stable state can be achieved if the aggregate happens to reach a state of retrograde rotation, with $w_z \sim -(1-2)\Omega$. In this case the aggregate has a droplet-like shape, in contrast to the roughly ellipsoidal shape of synchronously rotating aggregates. Some long-duration simulations in (Salo, 1995, see its Fig. 17b) apparently suffered such an artificial behavior, escaping our attention at the time the paper was written (this does not affect any of the conclusions of the paper). Nevertheless, this retrograde rotation is an artifact caused solely by accumulated numerical errors, and has probably no physical significance.

The treatment of gravity can be easily improved by including the linear term to the force calculations. In this case the leading energy error term becomes

$$\Delta\dot{E}_2 = \frac{1}{24}\Delta T^2 \sum_{\substack{j=1\\ j\neq i}}^{N} -\frac{Gm_i m_j}{r_{ij}^3}\big\{\vec{A}_{ij}\cdot\vec{V}_{ij} - 6(\vec{V}_{ij}\cdot\vec{R}_{ij}) \times r_{ij}^{-2}v_{ij}^2 + \big[-3\big(v_{ij}^2 + \vec{R}_{ij}\cdot\vec{A}_{ij}\big)r_{ij}^{-2} + 15(\vec{V}_{ij}\cdot\vec{R}_{ij})^2 r_{ij}^{-4}\big](\vec{V}_{ij}\cdot\vec{R}_{ij})\big\}. \quad \text{(A.8)}$$

Again, considering a spherical aggregate with $\vec{V}_{ij}\cdot\vec{R}_{ij} \approx 0$, the only remaining term is proportional to $\vec{A}_{ij}\cdot\vec{V}_{ij}$, reducing to $\Omega^2(3\dot{x}_{ij}x_{ij} - \dot{z}_{ij}z_{ij})$, as the contribution from the aggregate gravity and the Coriolis term of the central force field vanish. For small oscillations around the radially aligned equilibrium orientation this term is strictly periodic. The same appears to be true also for the other terms in Eq. (A.8) even if small non-zero $\vec{V}_{ij}\cdot\vec{R}_{ij}$ is allowed. Thus, $\Delta\dot{E}_2$ does not introduce secular change of energy, the secular error being proportional to ΔT^3.

Naturally, any Taylor expansion fails for particles experiencing an impact during ΔT (corresponds to a discontinuity in their velocities), in which case the linear expansion is not any better approximation than using constant forces. Therefore, a further refinement of the force calculation was also tested: the nearby particle pairs prone to collide during the step were excluded from the calculation of force expansions and were treated separately by a 4-order RK4. However, in practice no difference was seen in comparison to using linear force expansion for all particles, except considerably increased CPU time consumption.

To illustrate the practical differences with the two degrees of approximations, Fig. 13 compares the fate of aggregates (in terms of their spin) in simulations with different timesteps ΔT, both with the previous method and with the linear approximation. The main purpose is, besides indicating the

reliability of the improved approximation, to warn the potential users of the weaknesses of the previous gravity calculation method.

References

Aarseth, S.J., 1972. Direct integration methods of the *N*-body problem. In: Lecar, M. (Ed.), Gravitational *N*-Body Problem. In: Proceedings of IAU Colloq., vol. 10, pp. 373–387.

Aggarwal, H.R., Oberbeck, V.R., 1974. Roche limit of a solid body. Astrophys. J. 191, 577–588.

Araki, S., 1991. The dynamics of dense particle disks. III. Dense and spinning particle disks. Icarus 90, 139–171.

Barbara, J.M., Esposito, L.W., 2002. Moonlet collisions and the effects of tidally modified accretion in Saturn's F ring. Icarus 160, 161–171.

Bosh, A.S., Rivkin, A.R., 1996. Observations of Saturn's inner satellites during the May 1995 ring-plane crossing. Science 272, 518–521.

Bridges, F.G., Hatzes, A., Lin, D.N.C., 1984. Structure, stability and evolution of Saturn's rings. Nature 309, 333–335.

Bridges, F.G., Supulver, K.D., Lin, D.N.C., 2001. Energy loss and aggregation processes in low speed collision of ice particles coated with frosts or methanol/water mixtures. In: Pöschel, T., Luding, S. (Eds.), Granular Gases. Lecture Notes in Phys., vol. 564. Springer-Verlag, Berlin, pp. 153–183.

Chandrasekhar, S., 1969. Ellipsoidal Figures of Equilibrium. The Silliman Foundation Lectures. Yale Univ. Press, New Haven.

Charnoz, S., Brahic, A., Ferrari, C., Grenier, I., Roddier, F., Thebault, P., 2001. Detection of arcs in Saturn's F ring during the 1995 Sun ring-plane crossing. Astron. Astrophys. 365, 214–221.

Daisaka, H., Ida, S., 1999. Spatial structure and coherent motion in dense planetary rings induced by self-gravitational instability. Earth Planets Space 51, 1195–1213.

Daisaka, H., Tanaka, H., Ida, S., 2001. Viscosity in a dense planetary ring with self-gravitating particles. Icarus 154, 296–312.

Davis, R.D., Weidenschilling, S.J., Chapman, C.R., Greenberg, R., 1984. Saturn ring particles as dynamic ephemeral bodies. Science 224, 744–747.

Dilley, J.P., 1993. Energy loss in collisions of icy spheres: loss mechanism and size-mass dependence. Icarus 105, 225–234.

French, R.G., Nicholson, P.D., 2000. Saturn's rings II. Particle sizes inferred from stellar occultation data. Icarus 145, 502–523.

Goldreich, P., Tremaine, S., 1978. The velocity dispersion in Saturn's rings. Icarus 34, 227–239.

Hämeen-Anttila, K.A., Salo, H., 1993. Generalized theory of impacts in particulate systems. Earth Moon Planets 62, 47–84.

Julian, W.H., Toomre, A., 1966. Non-axisymmetric responses of differentially rotating disks of stars. Astrophys. J. 146, 810–830.

Longaretti, P.-Y., 1989. Saturn's main ring particle size distribution: an analytical approach. Icarus 81, 51–73.

Marouf, E.A., Tyler, G.L., Zebker, H.A., Simpson, R.A., Eshleman, V.R., 1983. Particle size distribution in Saturn's rings from Voyager I radio occultation. Icarus 54, 189–211.

McGhee, C.A., Nicholson, P.D., French, R.G., Hall, K.J., 2001. HST observations of saturnian satellites during the 1995 ring plane crossing. Icarus 152, 282–315.

Morishima, R., Salo, H., 2004. Spin rates of small moonlets embedded in planetary rings. I. Three body calculations. Icarus 167, 330–346.

Nicholson, P.D., Showalter, M.R., Dones, L., French, R.G., Larson, S.M., Lissauer, J.J., McGhee, C.A., Seitzer, P., Sicardy, B., Danielson, G.E., 1996. Observations of Saturn's ring-plane crossing in August and November 1995. Science 272, 509–516.

Ohtsuki, K., 1993. Capture probability of colliding planetesimals: dynamical constraints on accretion of planets, satellites, and ring particles. Icarus 106, 228–246.

Ohtsuki, K., 1999. Evolution of particle velocity dispersion in a circumplanetary disk due to inelastic and gravitational interactions. Icarus 137, 152–177.

Ohtsuki, K., Emori, H., 2000. Local *N*-body simulations for the distribution and evolution of particle velocities in planetary rings. Astron. J. 119, 403–416.

Porco, C.C., Throop, H.B., Richardson, D.C., 2001. Light scattering in Saturn's rings: basic disk properties and the A ring azimuthal asymmetry. Bull. Am. Astron. Soc. 33, 1091. Abstract.

Poulet, F., Sicardy, B., Nicholson, P.D., Karkoschka, E., Caldwell, J., 2000. Saturn's ring-plane crossings of August and November 1995: a model for the new F-ring objects. Icarus 144, 135–148.

Richardson, D.C., 1994. Tree code simulations of planetary rings. Mon. Not. R. Astron. Soc. 269, 439–511.

Roddier, F., Roddier, C., Brahic, A., Dumas, C., Graves, J.E., Northcott, M.J., Owen, T., 2000. Adaptive optics observations of Saturn's ring plane crossing in August 1995. Icarus 143, 299–307.

Salo, H., 1987. Numerical simulations of collisions between rotating particles. Icarus 70, 37–51.

Salo, H., 1991. Numerical simulations of dense collisional systems. Icarus 90, 254–270.

Salo, H., 1992a. Numerical simulations of dense collisional systems. II. Extended distribution of particle sizes. Icarus 96, 85–106.

Salo, H., 1992b. Gravitational wakes in Saturn's rings. Nature 359, 619–621.

Salo, H., 1995. Simulations of dense planetary rings. III. Self-gravitating identical particles. Icarus 117, 287–312.

Salo, H., 2001. Numerical simulations of collisional dynamics of planetary rings. In: Pöschel, T., Luding, S. (Eds.), Granular Gases. Lecture Notes in Phys., vol. 564. Springer-Verlag, Berlin, pp. 330–349.

Salo, H., Karjalainen, R., 1999. Dynamical and photometric modeling of azimuthal brightness asymmetry in Saturn's rings. Bull. Am. Astron. Soc. 31, 1160. Abstract.

Salo, H., Karjalainen, R., 2003. Photometric modeling of Saturn's rings I. Monte Carlo method and the effect of nonzero volume filling factor. Icarus 164, 428–460.

Salo, H., Schmidt, J., Spahn, F., 2001. Viscous overstability in Saturn's B-ring. I. Direct simulations and measurement of transport coefficients. Icarus 153, 295–315.

Salo, H., Karjalainen, R., French, R.G., 2004. Photometric modeling of Saturn's rings II. Azimuthal asymmetry in reflected and transmitted light. Icarus 170, 70–90.

Schmidt, J., Salo, H., Petzschmann, O., Spahn, F., 1999. Vertical distribution of temperature and density in a planetary ring. Astron. Astrophys. 345, 646–652.

Schmidt, J., Salo, H., Spahn, F., Petzschmann, O., 2001. Viscous overstability in Saturn's B-ring. II. Hydrodynamic theory and comparison to simulations. Icarus 153, 316–331.

Showalter, M.R., 1998. Detection of centimeter-sized meteoroid impact events in Saturn's ring. Science 282, 1099–1102.

Showalter, M.R., Nicholson, P.D., 1990. Saturn's rings through a microscope: particle size constraints from the Voyager PPS scan. Icarus 87, 285–306.

Spahn, F., Hertzsch, J.-M., Brilliantov, N.V., 1995. The role of particle collisions for the dynamics in planetary rings. Chaos Soliton. Fract. 5, 1945–1964.

Spahn, F., Schwarz, U., Kurths, J., 1997. Clustering of granular assemblies with temperature dependent restitution under Keplerian differential rotation. Phys. Rev. Lett. 78, 1596–1599.

Sremčević, M., Spahn, F., Duschl, W.J., 2002. Density structures in perturbed thin cold discs. Mon. Not. R. Astron. Soc. 337, 1139–1152.

Stewart, G.R., Lin, D.N.C., Bodenheimer, P., 1984. Collision-induced transport processes in planetary rings. In: Greenberg, R., Brahic, A. (Eds.), Planetary Rings. Univ. of Arizona Press, Tucson, pp. 447–512.

Supulver, K.D., Bridges, F.G., Lin, D.N.C., 1995. The coefficient of restitution of ice particles in glancing collisions: experimental results for unfrosted surfaces. Icarus 113, 188–199.

Toomre, A., 1964. On the gravitational stability of a disk of stars. Astrophys. J. 139, 1217–1238.

Toomre, A., Kalnajs, A.J., 1991. Spiral chaos in an orbiting patch. In: Sundelius, B. (Ed.), Dynamics of Disc Galaxies. Almquist-Wiksell, pp. 341–358.

Weidenschilling, S.J., Chapman, C.R., Davis, D., Greenberg, R., 1984. Ring particles: collisional interactions and physical nature. In: Greenberg, R., Brahic, A. (Eds.), Planetary Rings. Univ. of Arizona Press, Tucson, pp. 367–415.

Wisdom, J., Tremaine, S., 1988. Local simulations of planetary rings. Astron. J. 95, 925–940.